AGU PUBLICATIONS

Tectonics

RESEARCH ARTICLE
10.1002/2015TC004070

Key Points:
- The 80 km long section of the Longriqu fault could rupture as a whole during earthquake
- The inventory of offsets along fault shows evidence for nine past earthquakes
- The Longriqu fault zone follows a characteristic slip model with a ~4 m coseismic slip

Correspondence to:
C. Ansberque,
ansberque@cerege.fr

Citation:
Ansberque, C., O. Bellier, V. Godard, C. Lasserre, M. Wang, R. Braucher, B. Talon, J. de Sigoyer, X. Xu, and D. L. Bourlès (2016), The Longriqu fault zone, eastern Tibetan Plateau: Segmentation and Holocene behavior, *Tectonics*, *35*, doi:10.1002/2015TC004070.

Received 3 NOV 2015
Accepted 26 JAN 2016
Accepted article online 29 JAN 2016

The Longriqu fault zone, eastern Tibetan Plateau: Segmentation and Holocene behavior

Claire Ansberque[1], Olivier Bellier[1], Vincent Godard[1], Cécile Lasserre[2], Mingming Wang[3], Régis Braucher[1], Brigitte Talon[4], Julia de Sigoyer[2], Xiwei Xu[5], and Didier L. Bourlès[1]

[1]Aix-Marseille Université, IRD, CNRS, CEREGE UM34, Aix-en-Provence, France, [2]Université Grenoble Alpes, CNRS, UMR 5275, ISTerre, Grenoble, France, [3]Institute of Sedimentary Geology, Chengdu University of Technology, Chengdu, China, [4]Aix-Marseille Université, Institut Méditerranéen d'Ecologie et de Paléoécologie, IRD, CNRS, UMR 7263, Marseille, France, [5]Institute of Geology, China Earthquake Administration, Beijing, China

Abstract The dextral Longriba fault system (LFS), ~300 km long and constituting of two fault zones, has recently been recognized as an important structure of the eastern Tibetan plateau (Sichuan province), as it accommodates a significant amount of the deformation induced by the ongoing Indo-Asian collision. Although previous paleoseismological investigations highlighted its high seismogenic potential, no systematic quantification of the dextral displacements along the fault system has been undertaken so far. As such information is essential to appraise fault behavior, we propose here a first detailed analysis of the segmentation of the Longriqu fault, the northern fault zone of the LFS, and an offset inventory of morphological features along the fault, using high-resolution *Pleiades* satellite images. We identify six major segments forming a mature fault zone. Offsets inventory suggests a characteristic coseismic displacement of ~4 m. Two alluvial fans, with minimum ages of 6.7 and 13.2 ka, respectively displaced by 23 ± 7 m and 40 ± 5 m, give an estimate of the maximal horizontal slip rate on the Longriqu fault of 3.2 ± 1.1 mm yr^{-1}. As a result, a minimum ~1340 year time interval between earthquakes is expected.

1. Introduction

Although the eastern margin of the Tibetan plateau undergoes deformation related to the ongoing Indo-Asian collision [*Molnar and Tapponnier*, 1977], it experiences slow intracontinental strain rates [e.g., *Shen et al.*, 2009]. For decades, a misinterpretation of the slow deformation, inferred from geodetic measurements, led to an important underestimation of the seismic hazard over this area [e.g., *Thompson et al.*, 2015]. The 2008 M_w 7.9 Wenchuan and 2013 M_w 7.0 Lushan earthquakes, which ruptured two main oblique reverse dextral faults in the Longmen Shan (Figure 1), testify of the high seismic potential of the eastern Tibetan margin. The 300 km long dextral Longriba fault system (LFS), located ~200 km northwest of the Longmen Shan and oriented parallel to the frontal range, has been recently identified as a major intracontinental structure [*Xu et al.*, 2008; *Shen et al.*, 2009; *Guo et al.*, 2015] (Figure 1). Paleoseismological studies suggest that the LFS could produce $M_w > 7$ earthquakes [*Xu et al.*, 2008; *Ren et al.*, 2013a, 2013b]. However, the seismogenic behavior of the LFS remains presently poorly known: no detailed segmentation map has been produced at local scale (~10 km down to 10 m), and no systematic quantification of along-fault coseismic or cumulative horizontal displacements has been undertaken.

Fault segmentation mapping is an essential preliminary step in understanding fault maturity and behavior. Fault segmentation can affect rupture initiation, propagation, and arrest, and thus earthquake magnitude and slip distribution, with slip models that may differ from one segment to another [e.g., *Schwartz and Coppersmith*, 1984; *Walsh and Watterson*, 1988; *Sibson*, 1989; *Wells and Coppersmith*, 1994; *Bellier et al.*, 1997]. Simultaneously, inventories of offset geomorphological markers can provide valuable insights into the long-term, along-strike fault slip distribution. Several studies show that multiscale displacement inventories allow to decipher single-event slip from cumulative displacements [e.g., *Barka*, 1996; *van der Woerd et al.*, 2002; *Zielke et al.*, 2010, 2015; *Klinger et al.*, 2011]. Moreover, the along-strike fault cumulative displacement pattern can constrain whether or not fault segments are independently rupturing during earthquakes [e.g., *Schwartz and Coppersmith*, 1984; *Klinger et al.*, 2005; *Ren et al.*, 2015]. Such information on geometrical and displacement characteristics of faults is important to derive generic properties and improve our understanding of rupture process and seismic cycle [e.g., *Wesnousky*, 2008; *Manighetti et al.*, 2005].

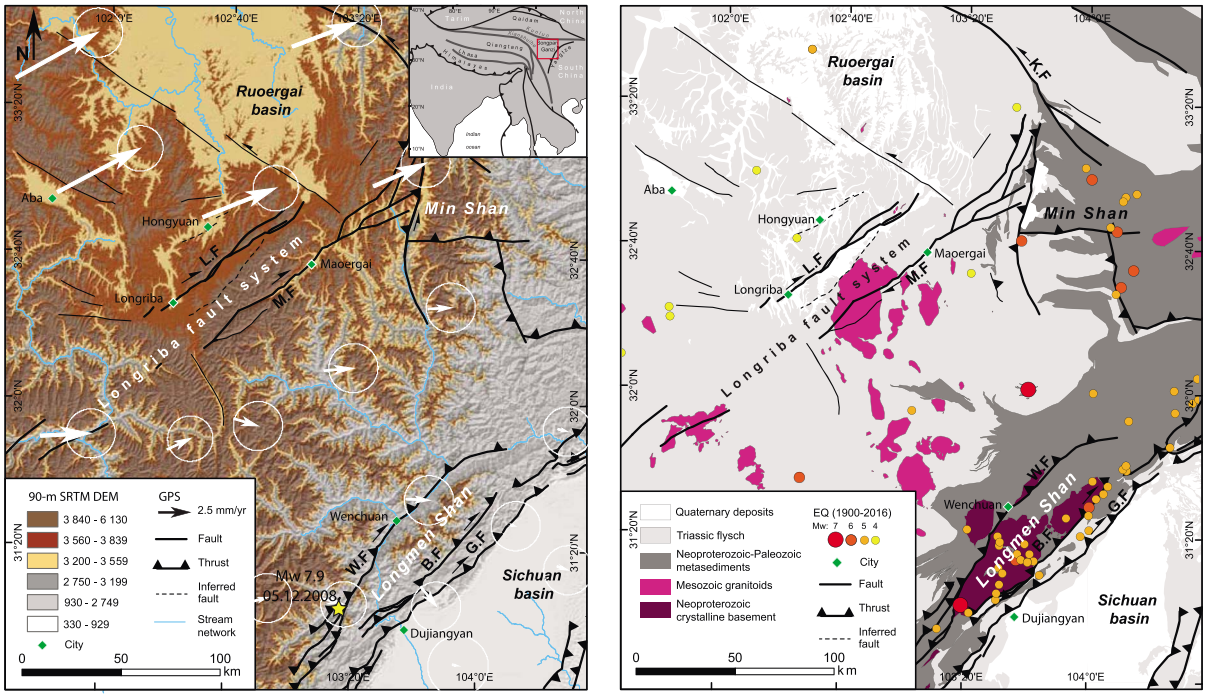

Figure 1. (left) Shaded elevation model of the eastern Tibetan plateau. Arrows are GPS velocities (error ellipses represent 70% confidence) referred to the Sichuan basin [*Shen et al.*, 2009]. (right) Structural map. Earthquakes come from the U.S. Geological Survey catalog. Seismic events of M_w4 were plotted only nearby the LFS area to avoid the M_w4 replicates associated to the Wenchuan and Lushan earthquakes. B.F: Beichuan fault. G.F: Guanxian fault. L.F: Longriqu fault. M.F: Maoergai fault. T.F: Tazang fault. W.F: Wenchuan fault. Bold lines represent active faults.

Laser techniques and satellite image analysis of fault zone morphology have highly improved the quantification of earthquake-related displacements along faults [*Siame et al.*, 1996; *Bellier et al.*, 2001; *Fu et al.*, 2004; *Bürgmann et al.*, 2006; *Klinger et al.*, 2011; *Gold et al.*, 2013; *Ren et al.*, 2015]. Along strike-slip faults, where human and climatic impacts are limited over a short timescale, surface rupture and associated geomorphic features can be remarkably preserved and mapped from such approaches. The systematic use of high-resolution images to retrieve fault slip history and distribution has been developed along the high slip rate San Andreas fault, where warm and dry climatic conditions favor the preservation of displaced geomorphic marker [e.g., *Wallace*, 1968; *Gaudemer et al.*, 1989; *Arrowsmith and Zielke*, 2009]. This method has been increasingly applied to the main seismogenic strike-slip faults of Asia [*van der Woerd et al.*, 2002; *Dominguez et al.*, 2003; *Harkins et al.*, 2010; *Klinger et al.*, 2011]. However, as paleoclimate changes are not evenly recorded along Asian faults, the conditions in which offsets form and evolve remain poorly understood. Likewise, the interplay between climatic changes and fault slip during the seismic cycle remains an opened question [*Heki*, 2001; *Hetzel and Hampel*, 2005, 2006; *Grant Ludwig et al.*, 2010; *Zielke et al.*, 2010; *Godard and Burbank*, 2011; *Steer et al.*, 2014].

In order to map the LFS segmentation at 10^3 down to 1 m scale, we analyze high-resolution (50 cm pixel size) images, acquired by *Pleiades* satellites. We focus here on the northern 80 km long section of the LFS: the Longriqu fault (Figure 2). We first map the Longriqu fault segments, then we systematically measure dextral displacements recorded by geomorphic markers, mostly stream channels crossing the fault perpendicularly, to assess if we can decipher the coseismic displacement of past earthquakes. Sampling and dating of displaced alluvial fans at two sites allow us to estimate a maximum dextral slip rate along the Longriqu fault, which we compare with geodetically determined short-term slip rates [*Shen et al.*, 2009] and previously derived Quaternary dextral slip rate [*Ren et al.*, 2013a, 2013b].

2. Seismotectonic and Geomorphological Settings

2.1. The Longmen Shan and the Longriba Fault System

The Longmen Shan and the LFS are important active structures of the eastern Tibet that find their origin during the Paleozoic Era [*Guo et al.*, 2015] (Figure 1). *Guo et al.* [2015] suggest that both structures formed

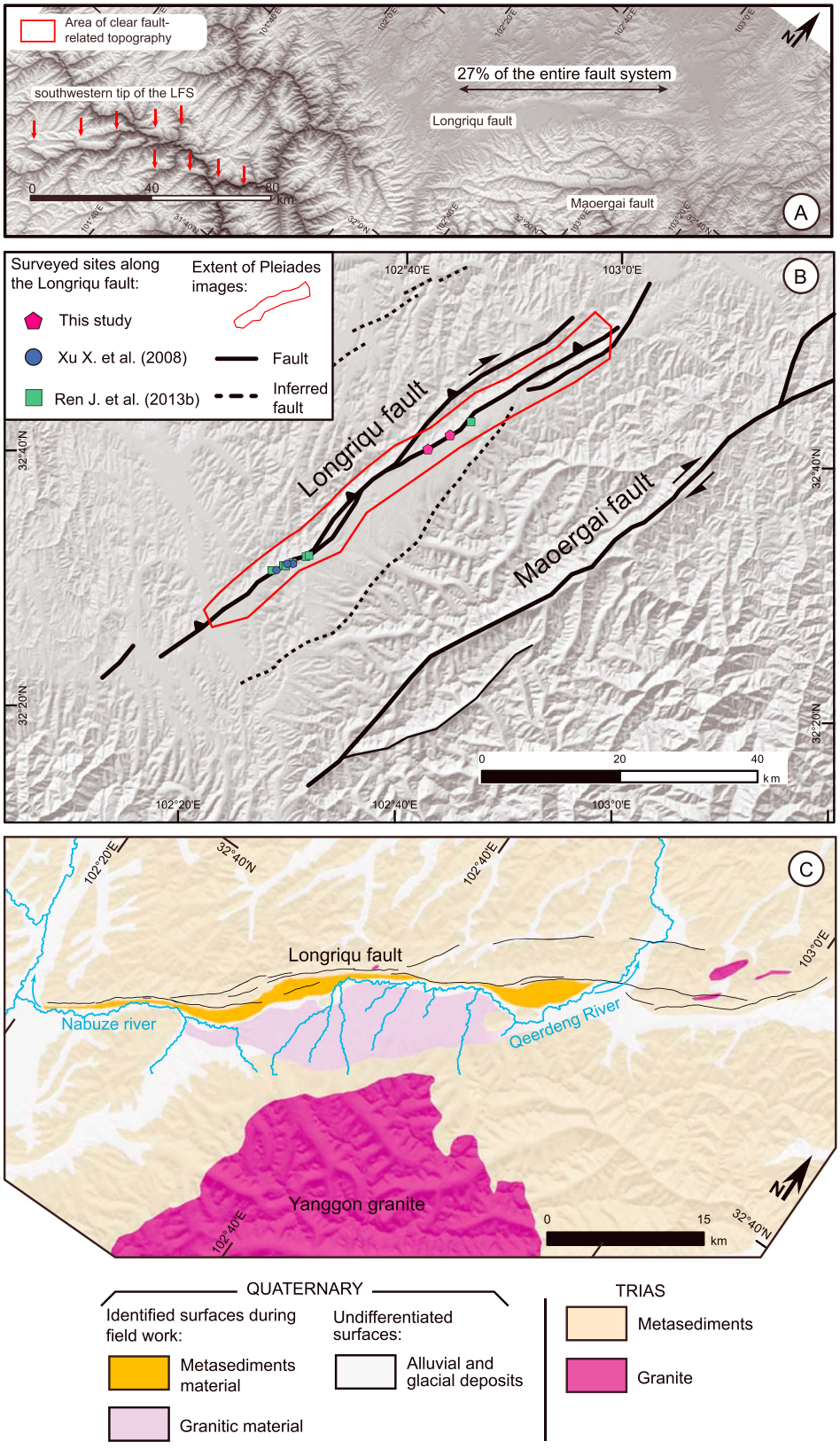

Figure 2. (a) Ninety meter SRTM DEM along the 80 km long well-expressed LFS. Red arrows highlight the southwestern zones of the LFS. (b) Regional-scale view of the two LFS zones (SRTM DEM). (c) Geomorphological map of the study area.

when the eastern edge of the Yangtze craton, which lies underneath from the LFS to the Sichuan basin, was a passive margin [e.g., *Roger et al*., 2004; *Harrowfield and Wilson*, 2005]. The Longmen Shan and the LFS were inverted during the closure of the Songpan Garze basin (Middle Triassic) [*Roger et al*., 2008; *Pullen et al*., 2008; *Guo et al*., 2015]. The Longmen Shan, which represents a topographic boundary between the Sichuan basin (500 m above sea level (asl)) and the Tibetan plateau (~4000 m asl), is composed of three main transpressive NE trending faults: the Wenchuan, Beichuan, and Guanxian faults, accommodating most of the convergence between the basin and the plateau (Figure 1). The LFS, parallel to the Longmen Shan, is made of two dextral faults: the Longriqu and Maoergai faults, ~50° trending and NW dipping [*X. Guo et al*., 2013].

Over long timescale (>1 Ma), thermochronological data depict multiple growth phases of the Longmen Shan with a slow and steady exhumation stage during early Cenozoic Era and rapid exhumation pulses during late Oligocene and Miocene [*Wang et al*., 2012; *Tian et al*., 2013]. Across the LFS, because of the lack of data, the million year timescale deformation history cannot be assessed. However, the LFS was reactivated during Pleistocene time [*Xu et al*., 2008; *Ren et al*., 2013a]. Geodetic studies indicate that shortening across the Longmen Shan is ~1.4 mm yr^{-1} (slip component normal to the fault strike) with a lateral slip rate of ~1.7 mm yr^{-1} [*Shen et al*., 2009]. In contrast, the LFS accommodates a shortening rate of ~0.7 mm yr^{-1} [*Xu et al*., 2008] but about 5 ± 1 mm yr^{-1} of lateral slip rate (slip component parallel to the fault strike) [*Xu et al*., 2008; *Shen et al*., 2009]. The LFS strike and its significant dextral slip rate suggest that this fault system play an important role in strain partitioning, accommodating part of the oblique motion of the Aba block (lying under the Ruoergai basin), with respect to the Sichuan basin [*Shen et al*., 2009; *Ren et al*., 2013b].

The LFS runs over ~300 km from the Kunlun fault to the north, to the Xianshuihe fault to the south [*Shen et al*., 2009] (Figure 1). However, the morphologically well-expressed part of the LFS is located directly south of the Ruoergai basin and represents less than 30% of the entire fault system (Figure 2a). The northeastern part of the Longriqu fault runs into the Songpan Ganze flysch (metasediments) and Quaternary fluvioglacial deposits (Figures 2b and 2c). A significant relief is present on the northwest side of the Longriqu fault, while a large basin extends south up to the Maoergai fault (Figure 2b). Over the late Quaternary, the Maoergai fault behaved as a pure dextral fault, and three ruptures have been documented at ~8510, ~7100, ~5170 cal yr B.P. [*Ren et al*., 2013a]. The dextral slip rate of the Maoergai fault is estimated between 0.7 mm yr^{-1} (since ~9.5 ka) to 2.1 (at ~21 ka). Four earthquakes have been reported along the Longriqu fault at 17,830, 13,000, 11,100, and 5080 cal yr B.P., with mostly dextral slip and a minor thrust component up to 1.2 m of apparent coseismic throw [*Ren et al*., 2013b]. *Ren et al*. [2013b] used high-resolution DEM for measuring local cumulative dextral displacements along the Longriqu fault, ranging from ~7 to ~50 m, and estimated a dextral slip rate ranging from 1.4 ± 0.3 (since ~11 ka) to 2.5 ± 0.4 mm yr^{-1} (at ~18 ka) with a small vertical slip rate of 0.1 ± 0.1 mm yr^{-1}. The average time interval between earthquakes on the LFS seem to be ~2000 years, and a clustered earthquakes model has been suggested [*Ren et al*., 2013b]. Tectonic and paleoseismological studies conducted across the two fault zones show that they can both produce earthquakes ranging from M_w 7 to 7.4 [*Xu et al*., 2008; *Ren et al*., 2013a, 2013b].

2.2. Geomorphological Settings

The Ruoergai basin—also called the Zoige basin—seems to be a tectonically controlled feature bounded to the south by the LFS and to the north by major sinistral NW trending faults, such as the Kunlun fault (Figure 1). The basin lies at ~3400 m (asl), covers about 30.000 km^2, and has a metasedimentary basement [*Jia et al*., 2010], which developed during Triassic [e.g., *Sengör*, 1985; *Mattauer et al*., 1992; *Roger et al*., 2010]. Over the Holocene, the basin has recorded a long lacustrine history [*Zhao et al*., 2011]. Currently, the combination of both southeast and southwest Asian monsoons contributes to supply rain water to the basin during summer periods [*Zhao et al*., 2011]. The mean annual precipitation rate is estimated to be around 580–860 mm [*Chen et al*., 1999]. Denudation rates derived near the LFS ranges from 0.04 to 0.1 mm yr^{-1} reflecting slow erosional processes [*Ansberque et al*., 2015]. As a result of its high elevation and low relief, the basin surface is covered by mountain meadows and bog soils in its western part [e.g., *Zhou et al*., 2002; *Zheng et al*., 2007; *Mischke and Zhang*, 2010; *Zhao et al*., 2011; *C. X. Guo et al*., 2013]. The latter started to develop during the Holocene climatic optimum around 9 to 5 ka (cal B.P.) [*Zheng et al*., 2007; *Mischke and Zhang*, 2010; *Zhao et al*., 2011]. During this stage, the weather was warm and wet, and the basin water level high enough to create a large flooded area and generate thick peat formation. Bog soils also developed further south within small catchments perpendicular to the Longriqu fault.

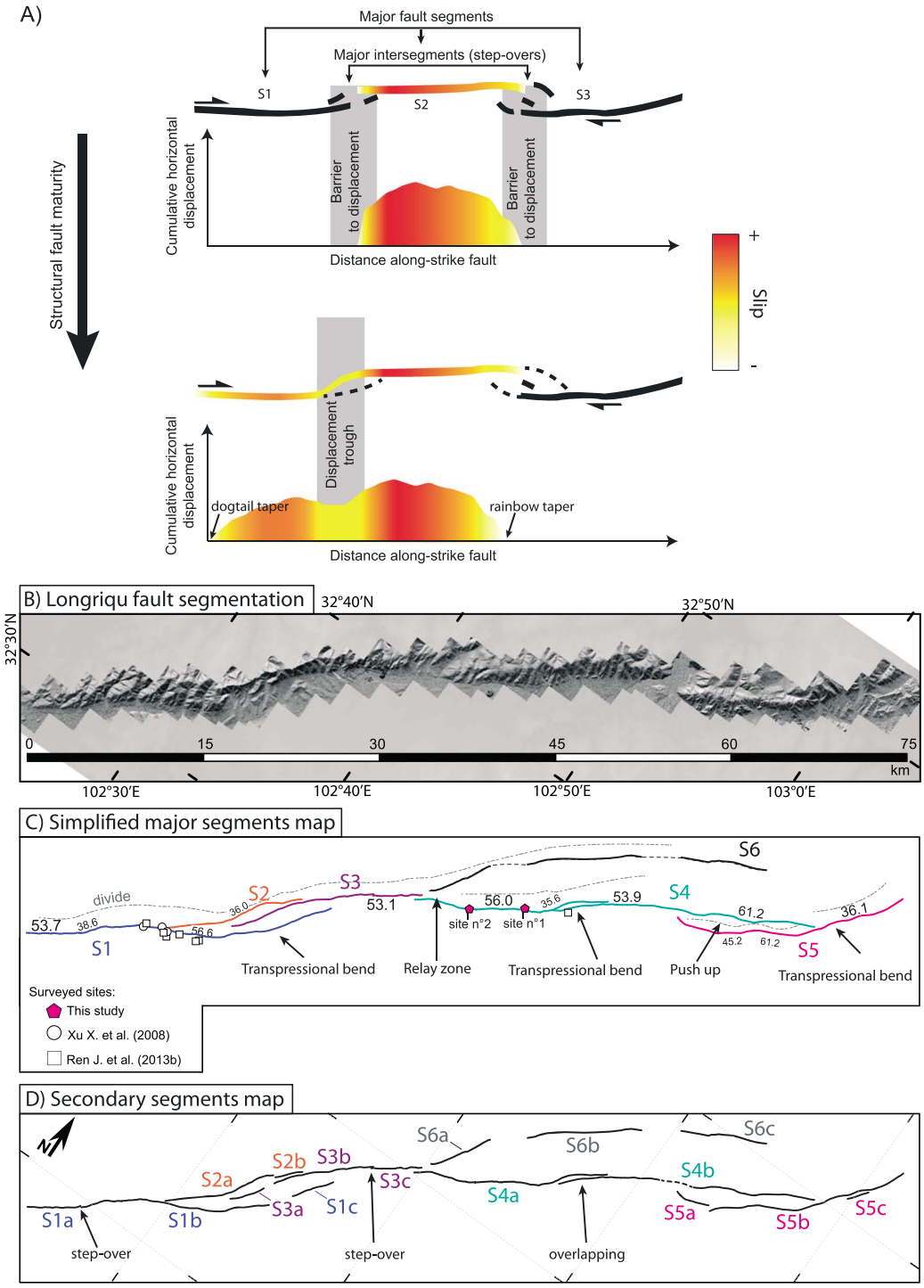

Figure 3. (a) Schematic fault segment organization and maturity evolution with associated slip distribution (modified from *Manighetti et al.* [2015]). (b) Shaded DEM derived from orthorectified Pleiades images. (c) Simplified major segments map (at scale of ~10 km). Numbers indicate the fault strike. Dash-dotted line locates the drainage divide. (d) Map of secondary segments.

Presently, the Ruoergai basin and the LFS are drained by the Yellow River system, which flows northward and incised the low relief-high elevation areas of the Plateau since Tertiary-Quaternary times [*Li et al.*, 1997; *Métivier et al.*, 1998; *Harkins et al.*, 2007]. The Longriqu fault is more specifically drained by the Qeerdeng river (Figure 2c). The latter runs along the fault strike over ~40 km. The alluvial plain associated with the river is

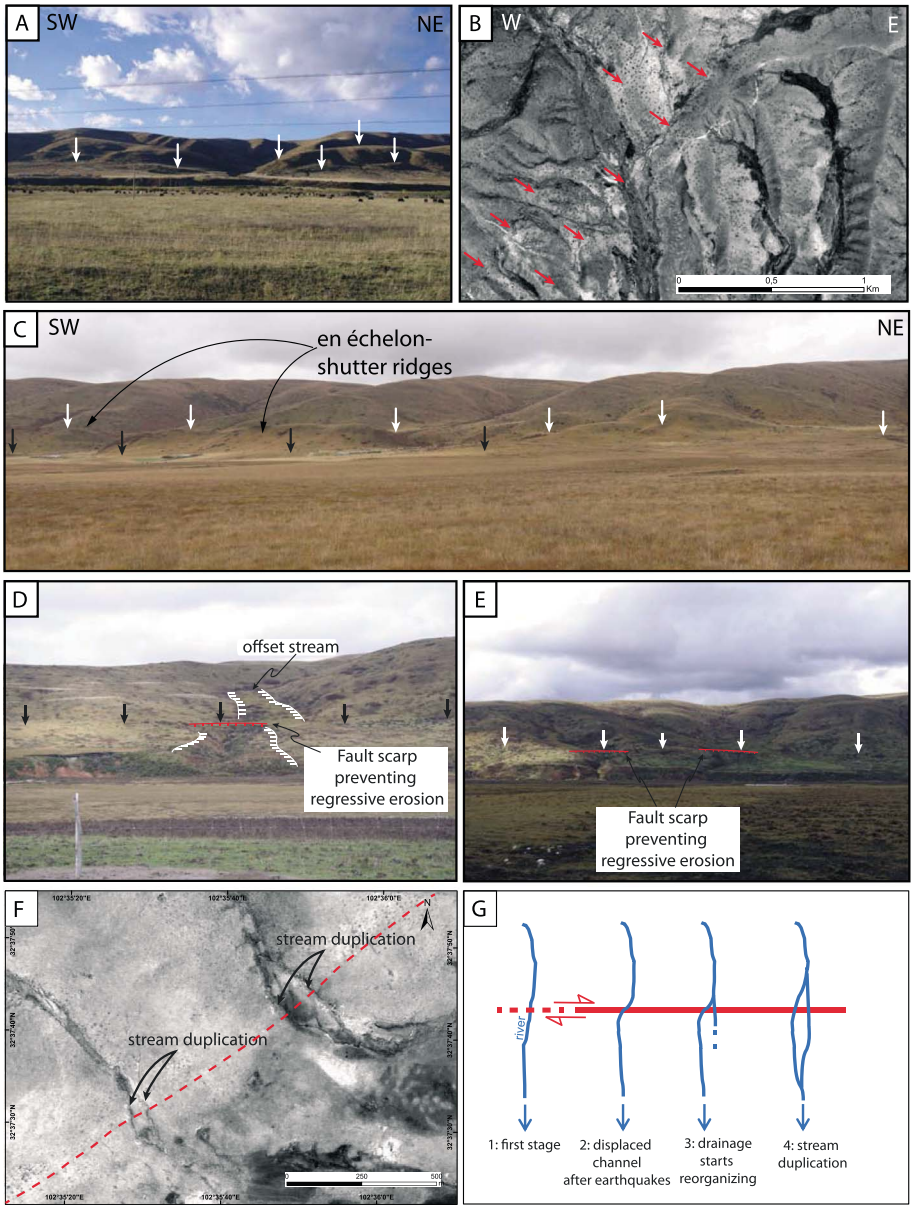

Figure 4. Observations of the Longriqu fault and its interaction with the topography (see Figure 2 for locations). (a) Field picture of the Longriqu fault. (b) Longriqu fault trace on orthorectified Pleiades images (underlined by red arrows). (c) Field picture of en échelon-shutter ridges. (d and e) Field pictures of sudden erosion stop controlled by the Longriqu fault. (f) Pleiades images showing streams duplication at the fault location. (g) Plausible explanation of streams duplication process through time.

~800 to 1.2 km wide and is bounded by two deposition surfaces. ESE and SE the river, the present-day slightly NW dipping surface is mainly composed of material coming from the erosion of the Yanggon granite (located ~8 km south the Qeerdeng River) (Figure 2c). This surface is ~15 m higher than the alluvial plain of the Qeerdeng River elevation. West the river (directly downstream the Longriqu fault) the deposition surface is slightly dipping toward the SE and is mainly composed of relatively angular schist and quartz pebbles, suggesting that most of these materials come from the hillslope (upstream of the Longriqu fault, where the relief is up to 400 m higher) to form a piedmont (Figure 2c). This surface is ~10 to 20 m above the alluvial plain. The Qeerdeng River is thus incising both this piedmont and the erosional deposits from the Yanggon granite but did not form major terraces within its alluvial plain. The river cuts the Longriqu relief in the northeast part of the fault and is probably associated to an antecedent drainage. The southwestern part of

Table 1. Segments of the Longriqu Fault

			Secondary Segments		
Major Segment Label	Length (km)	Mean Azimuthal Strike	Label	Length (km)	Mean Azimuthal Strike
S1	24.5	51.6	S1a	4.6	53.7
			S1b	16.3	52.6
			S1c	3.6	36.2
S2	12.0	40.6	S2a	9.6	39.4
			S2b	2.4	44.6
S3	16.0	50.0	S3a	3.0	37.1
			S3b	8.6	47.0
			S3c	4.4	55.6
S4	39.0	57.4	S4a	16.9	58.7
			S4b	22.1	56.1
S5	20.3	51.0	S5a	3.0	88.8
			S5b	17.3	42.4
			S5c	1.9	37.4
S6	22.7	46.8	S6a	5.5	35.7
			S6b	9.8	62.9
			S6c	7.4	49.5

the Longriqu fault is crossed cut by the Nabuze River, which could also be antecedent to the fault (Figure 2c), as suggested by *Ren et al*. [2013b] who estimated a 500 m offset of the river.

3. Fault Segmentation From Pleiades Satellite Imagery

3.1. Pleiades Images Processing

We used five stereo couples of Pleiades images to generate a high-resolution Digital Elevation Model (DEM) along the Longriqu fault trace using the ENVI 5.0 (EXELIS) software (Figure 2b). Original images are panchromatic, not orthorectified, with horizontal resolution of 50 cm. During the DEM processing, no ground control point has been used, and we relied on the Rational Polynomial Coefficient (RPC), included in the metadata of the Pleiades images. The derived DEM has an optimal horizontal resolution of 5 m and a vertical precision of ~10 m. Higher horizontal resolutions have been tested, but produce high surface roughness. The derived DEM was used to orthorectify the original Pleiades images under ArcMap 10.0 (ESRI) using the image's RPC. The segmentation analysis and offsets inventory were performed on the orthorectified Pleiades images.

3.2. Fault Segmentation

Segments and discontinuities identification is an important issue during fault analysis to assess the potential of the different segments to rupture all together or independently [e.g., *Aki*, 1984; *Schwartz and Coppersmith*, 1984; *Barka and Kadinsky-Cade*, 1988; *Klinger et al*., 2011] (Figure 3a). We provide here a detailed mapping of the Longriqu fault surface trace, from the analysis of orthorectified Pleiades images at a scale lower than 1:4000 (Figures 3b–3d). This mapping was also improved by field observations of right-lateral offsets, shutter ridges, sudden stop of the regressive erosion at the fault location, rivers widening, or streams duplication (Figure 4).

Along the 80 km long Longriqu fault, six major segments with length ranging from ~12 to ~35 km have been identified (Figure 3c and Table 1), separated by large (>100 m wide) geometric discontinuities such as bends, relay zones, and large overlaps. Segments are numbered S1–S6 from west to east. The mean strike of the Longriqu fault is ~54°. At 15 km along fault strike, segment S2 makes a ~36° significant strike change forming a large restraining bend between segment S1 and S3, which are oriented ~50° (Figure 3c). Segments S3, S4, and S6 branch off in a relay zone at ~35 km along fault strike. Segment S4 overlaps with segment S5 building a push-up into a restraining step over at ~55 km along fault strike, which is clearly distinguishable in the topography (Figures 3b, and 3c). The northeastern end of segment S5 corresponds to a restraining bend striking 36°. At least 12 secondary segments are identified ranging from 2 to 22 km and separated by small (<10 m wide) discontinuities such as step overs (Figure 3d and Table 1). Segments S1 and S3 are made of three secondary segments, segments S2 and S4 of two secondary segments, and segment S5 of three secondary segments. At 45 km along fault strike, segments S4a and S4b overlap each

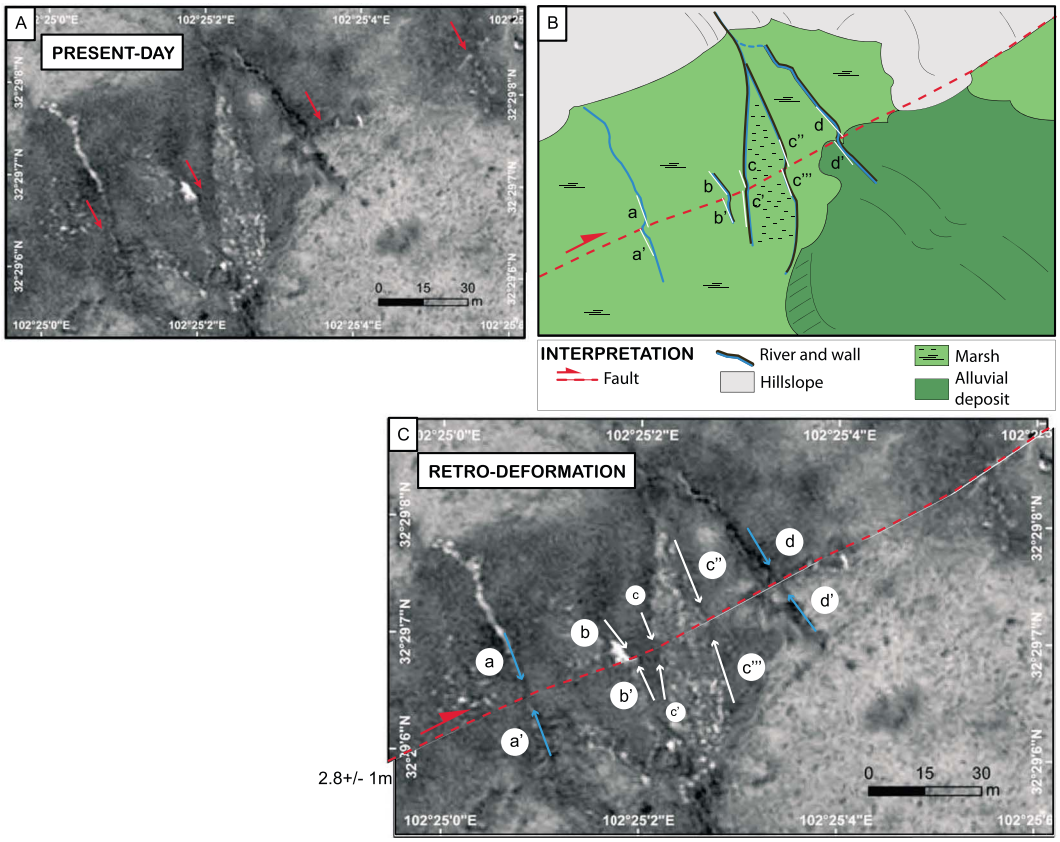

Figure 5. Example of smallest offsets measurement. (a) Orthorectified Pleiades images. Red arrows underline the fault. (b) Schematic interpretation. (c) Retrodeformation.

other forming a restraining bend (35°) (Figures 3c and 3d). We cannot present a high-resolution mapping of segment S6 due to the lack of Pleiades images in this area (Figures 2c and 3b). However, according to lower resolution satellite images (QuickBird, Advanced Spaceborne Thermal Emission and Reflection Radiometer (ASTER) and Shuttle Radar Topography Mission (SRTM)), we suggest the presence of three secondary segments along S6 (Figure 3b).

4. Offsets Distribution

4.1. Principle, Method, and Uncertainties

During a strike-slip fault rupture, all fault crossing features, such as stream channels, can be horizontally displaced. If the geomorphological conditions allow their preservation these features can be offset several times and thus record the cumulative displacement of several past earthquakes. The along-strike fault offset inventory would then reveal different sets of displacement values, which could represent successive coseismic offsets. Consequently, the smallest values are likely to be related to the last seismic rupture of the strike-slip fault, while sets of larger values correspond to cumulative displacements over several seismic cycles [e.g., *Wallace*, 1968; *Sieh and Jahns*, 1984; *McGill and Sieh*, 1991; *Zielke et al*., 2010, 2015; *Klinger et al*., 2011].

Providing a consistent and meaningful offsets inventory along a strike-slip fault is challenging as offset quantification depends on (i) the stream reconstruction on either side of the fault, (ii) the geomorphic markers type and preservation through time, and (iii) consistent manual measurements all along the fault. Several studies summarized procedures to properly measure offsets [*Ritz et al*., 1995; *van der Woerd et al*., 2002; *Cowgill*, 2007; *Zielke et al*., 2015]. Based on these previous studies and aware that the choice of the markers will feed back on the slip distribution and slip rate results, we measured only offset rivers and terrace risers (Figure 5). To minimize uncertainties associated to geomorphic features degradation and river widening, only rivers of similar width ranging from 1 to 20 m were picked. Limiting the measures to similar

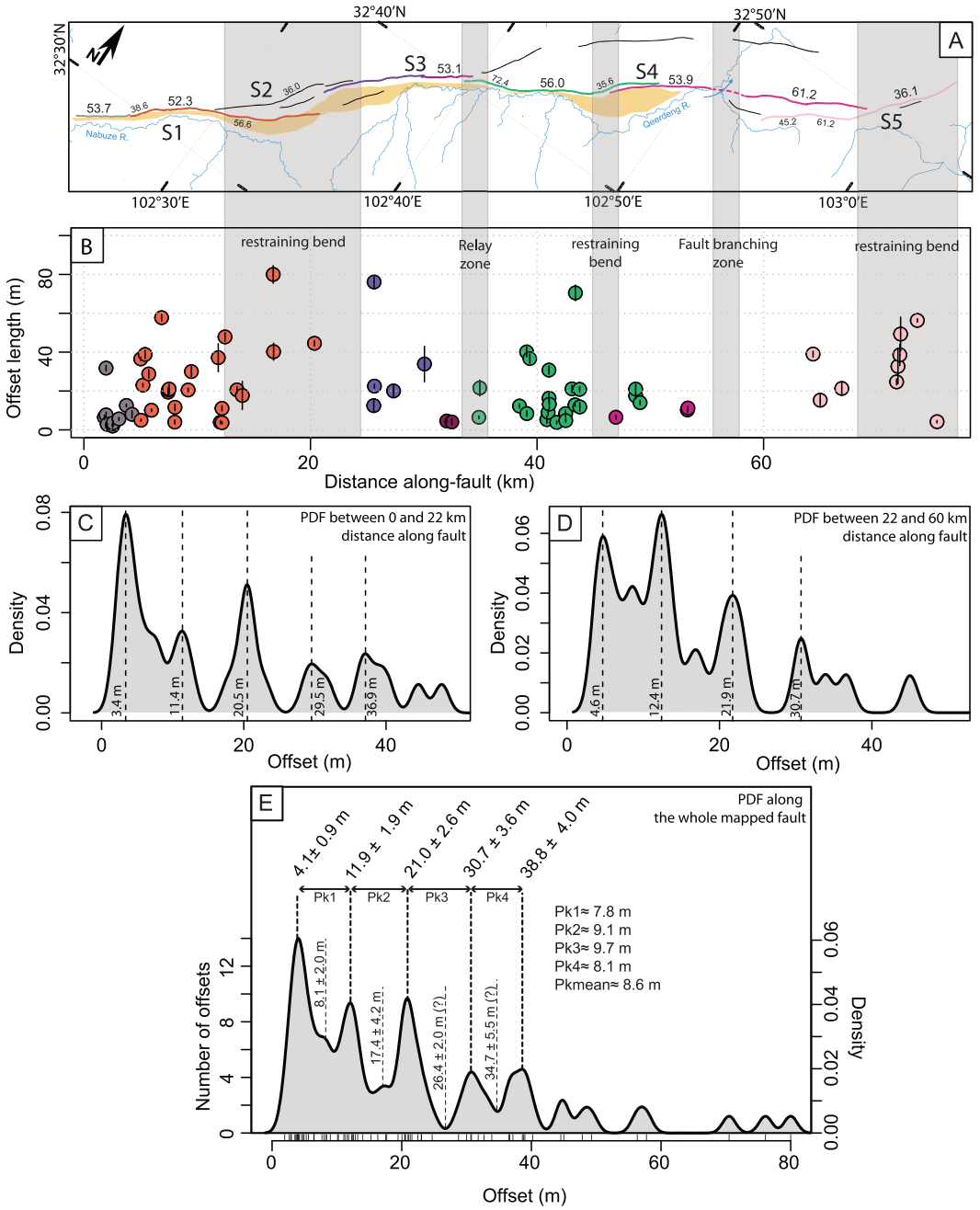

Figure 6. Offsets inventory along the Longriqu fault. (a) Segmentation map. Numbers refer to the fault strike. Quaternary deposits are represented in yellow, and river network with blue lines. (b) Along-fault offsets. Each point represents an offset channel. Colors refer to those of segments on Figure 6a. (c) Probability density function (PDF) of the offsets from 0 to 22 km along fault. (d) PDF of the offset from 22 to 60 km along fault. (e) PDF taking into account all offsets along fault, computed using a Gaussian kernel with a bandwidth of 1 m. The number of offsets is determined from the histogram.

types of markers allows to avoid potential uncertainties related to the marker size. This approach also limits the maximum range of displacements that can be measured. Indeed, cumulative displacements on a 10^1 to 10^4 ka timescales are preferentially recorded and preserved by large geomorphic markers (ridges, crests, staged terraces, and large rivers) than smaller rivers through time. As one of our main interests is to find the most recent coseismic offsets along the Longriqu fault, we did not select such large markers. We also retrodeformed the offsets to reconstruct the horizontally displaced past morphologies and check the

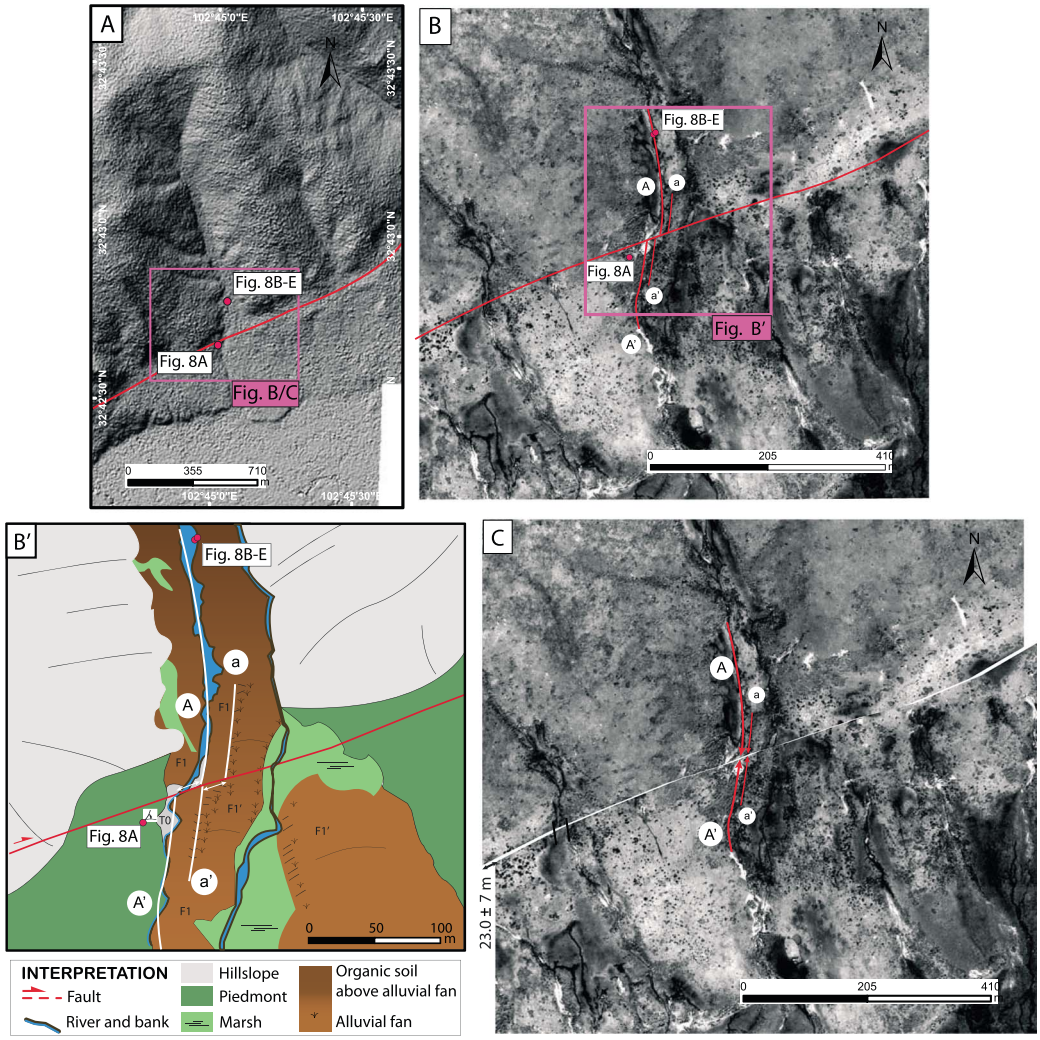

Figure 7. Site 1. (a) Hillshaded DEM from orthorectified Pleiades images. (b) Orthorectified Pleiades image zoomed on offset alluvial fan. (b′) Close up view of Figure 7b with interpretation. Marshes correspond to a thick level of peat covering the alluvial fan (see Figure 8). (c) retrodeformation of the measured displacements.

consistency between disconnected streams on either side of the fault (Figure 5). Field surveys have permitted us to observe different levels of terraces from modern deposits near the present-day river bed elevation (T0) to older and higher terraces. However the best-preserved risers corresponds to T1/T0 or F1(alluvial fan surface)/T0 transitions.

We attributed two uncertainties to the displacement measures. The first one is related to the image pixel size resolution. As Pleiades images have a horizontal resolution of 50 cm, minimum offset uncertainties are set to be systematically ± 1 m (50 cm are added on the two tips of the offset). The second uncertainty, added to the first one, represents the range of possible offset values best-fitting the retrodeformed morphology. This second uncertainty is statistically approached by measuring manually one offset several times. As most of the geomorphic markers are not fully preserved through time and degraded, uncertainties increase with offset values.

4.2. Offsets Inventory

Along the Longriqu fault, 74 offsets recorded by geomorphic markers have been measured (Figures 6a and 6b). They are well distributed along the fault, excepted in bends (Figures 6a and 6b). Offsets inventory along strike-slip fault can be analyzed with statistical methods [*Wallace*, 1968; *McGill and Sieh*, 1991; *van der Woerd et al.*, 2002; *Zielke et al.*, 2010, 2015; *Klinger et al.*, 2011]. In order to highlight the different ranges of offsets

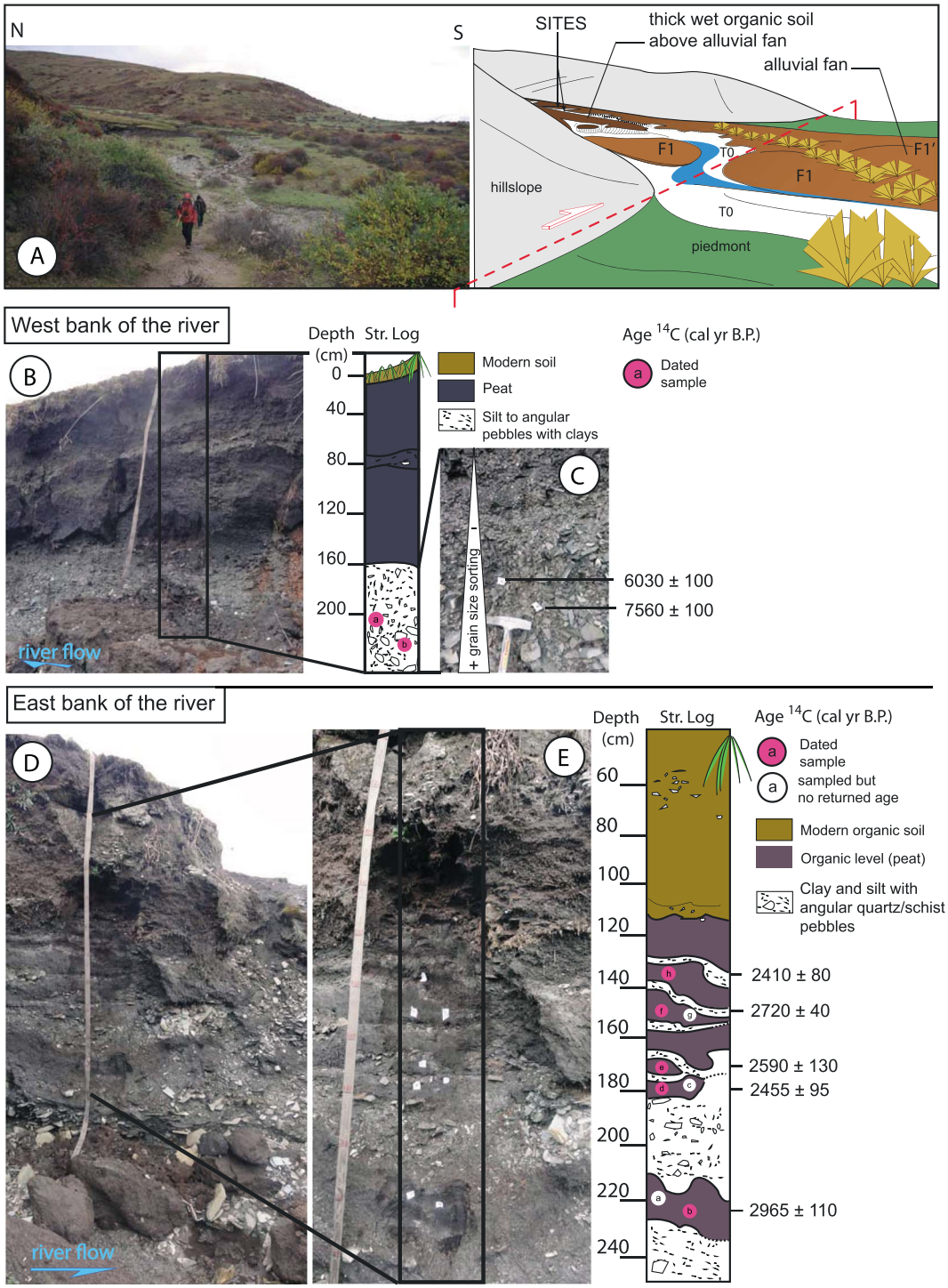

Figure 8. Illustration field view of Site 1 and stratigraphic log. (a) Photography of the displaced fan and associated interpretation (see Figure 7b′ for the view angle). (b and d) Views of the sampled surfaces on both sides of the river (west and east, respectively). (c and e) Respective zooms on sampled levels. Samples in (C) are associated to the top of the alluvial fan.

recorded along the Longriqu fault, displacements have been classified into a probability density (Gaussian kernel) function (PDF) (Figures 6c–6e). This approach, developed by *McGill and Sieh* [1991] allows deciphering the displacement ranges that are significantly represented along the fault. All measurements were made on ArcMap and the PDF was built on the R software.

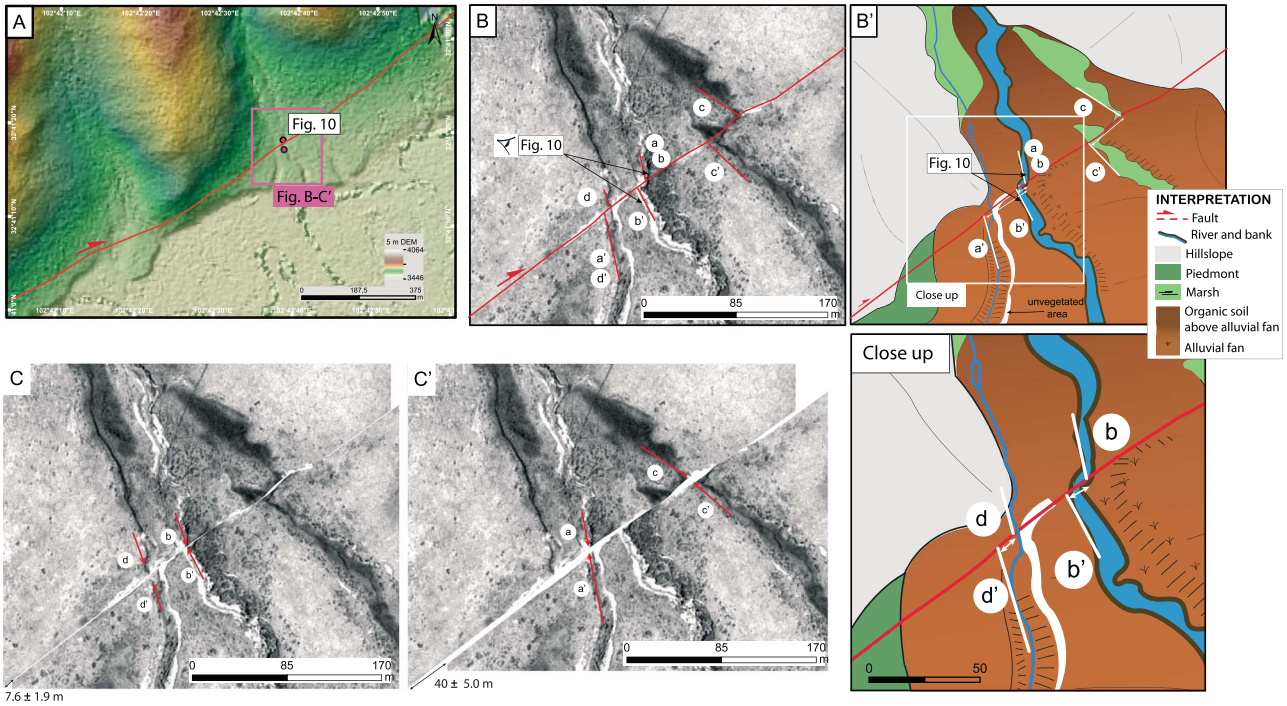

Figure 9. Site 2. (a) Hillshaded DEM from orthorectified Pleiades images. (b) Zoom on displaced alluvial surface. (b') interpretation of Figure 9b with zoom below (see white rectangle on Figure 9b' for the zoom location). (c and c') Retrodisplacement of the measured offset.

The PDF of the recorded offsets along the Longriqu fault displays evidence for five clearly distinct peaks, which we relate to five well-preserved channel offset ranges (Figures 6c–6e). Ranges of well-represented offsets are centered around 4.1 ± 0.9, 11.9 ± 1.9, 21.0 ± 2.6, 30.7 ± 3.6, and 38.8 ± 4.0 m (Figure 6e). We note that each peak value is close to a multiple of 4, with a peak-to-peak wavelength of ~9 m (Figure 6e).

Five slip rate estimates from ^{14}C and ^{10}Be dating numerous small alluvial fans, which developed at the outlet of most catchments, contribute to form the piedmont surface south of the Longriqu fault and have been horizontally displaced by the fault. In order to constrain the dextral slip rate of the Longriqu fault, we sampled and dated two of those horizontally displaced alluvial fans (Figures 7–10). We used radiocarbon (^{14}C) dating to constrain the age of the fan 1 deposit and the cosmogenic nuclide (^{10}Be) exposure dating to model the age of abandonment of the fan 2 surface, where organic material was rare.

4.3. Site 1 (32°42.792′N, 102°45.057′E)

Site 1 is located on segment S4a (~40 km along fault strike, Figure 3c) at the outlet of a catchment (Figure 7a) and corresponds to an alluvial fan ~630 m long and ~210 m wide covered by peat and vegetation. The alluvial fan exhibits a 23.0 ± 7.0 m offset recorded by two different markers (Figures 7b and 7c). Offsets have been estimated by realigning (i) the present-day river bed in the vicinity of the fault (AA′, Figures 7b and 7c) and (ii) F1/F1′ which corresponds to a slight topographic change in the alluvial fan mostly expressed downstream of the fault (aa′, Figures 7b′). The distinction between F1 and F1′ becomes unclear upstream of the fault (Figures 7b′ and 8a). We collected organic sediments and charcoals along vertical sections freshly exposed by the river downcutting into the apex of the alluvial fan 170 m upstream from the fault. The proximity of the alluvial fan source can lead to younger ages than those downstream, but no more favorable outcrop was present close to the fault (Figures 8b–8e). We tried to identify the botanical classes of the samples, but some of them could not be recognized (Table 2). The two sampling sites are ~15 m from each other. On the west bank of the river, in the alluvial fan deposit, two samples have been collected: a charcoal at 2 m depth and some plant remains at 2.20 m depth (Figures 8b and 8c). Radiocarbon ages of the two samples are 6030 ± 100 and 7560 ± 100 cal yr B.P., respectively (Table 2 and Figure 8c). Ages are derived from the accelerator mass spectrometry (AMS) facility at Poznan Radiocarbon Laboratory and have been calibrated using CALIB 7.0.4 (http://calib.qub.ac.uk/calib/download/) with the calibration curve IntCal13 [*Reimer et al.*, 2013].

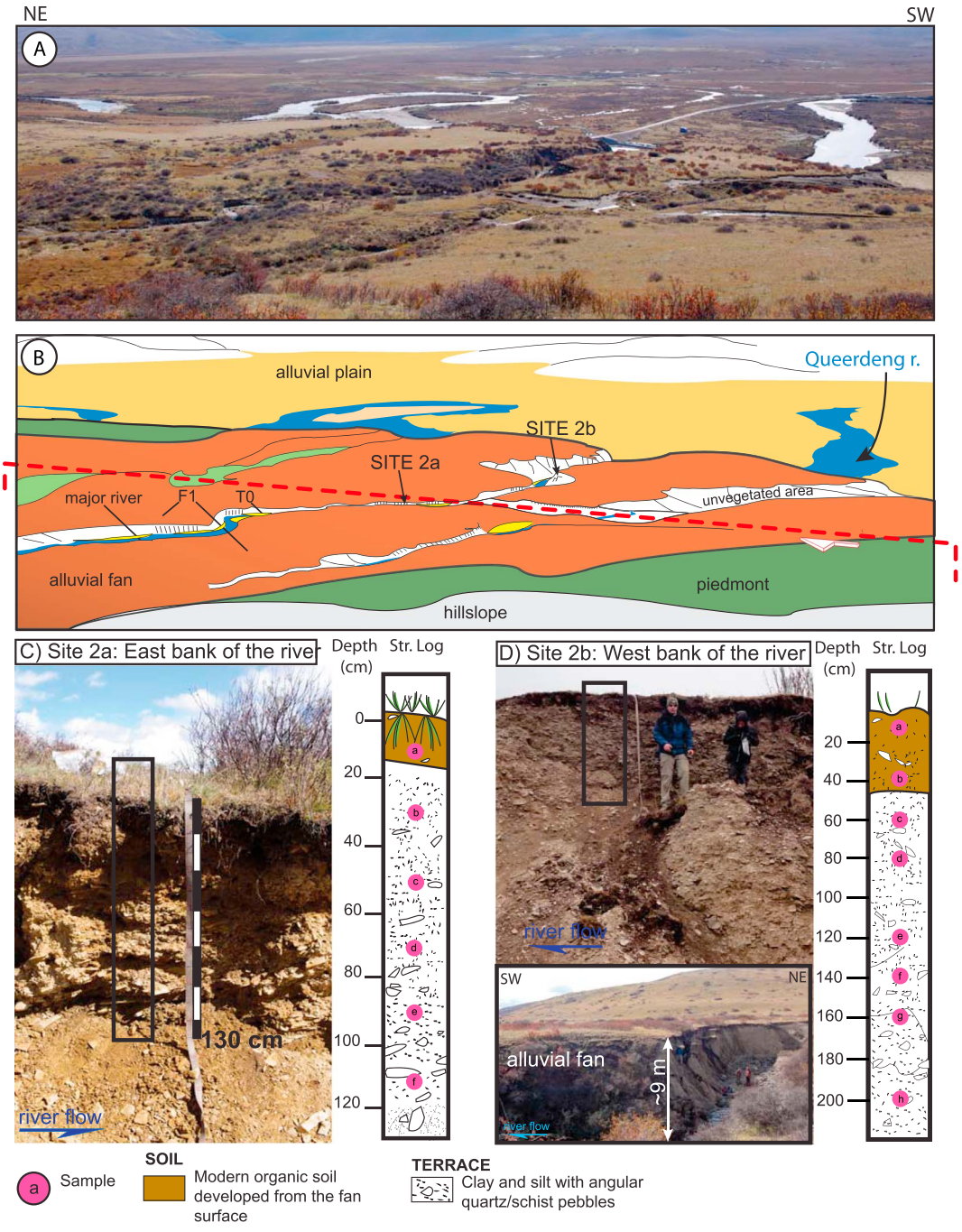

Figure 10. Illustration of Site 2 and stratigraphic log. (a) Photography of the displaced and sampled alluvial surface of Site 2 (see Figure 9b for the view angle) and (b) its interpretation. (c and d) Photographies and stratigraphic log of the east (Site 2a) and west (Site 2b) river bank, respectively.

The scatter between the two ages is large. However, as samples are only 20 cm from each other, we assume that such scatter is due to deposit reworking processes. Because these samples were extracted from very close to the top of the alluvial fan, we consider the samples average age (6795 ± 100 cal yr B.P.) to approximate the minimum age of the fan. Above the alluvial fan and especially in the fan apex area, a thick wet organic soil has developed, interspersed with thin fluvial layers suggesting changes in deposit dynamics (Figures 8d and 8e). Similar thick organic deposits have been analyzed in the Hongyuan valley, ~15 km farther north (Figure 1), described as peat, and dated between 9460 ± 70 and 1540 ± 40 cal yr B.P. from ~4 m to 25 cm

Table 2. Radiocarbon Ages

Bank	Sample ID	Sample Material	^{14}C Ages (Mean ± σ/cal yr B.P.)	Calibrated ^{14}C Ages (2σ) (cal yr B.P.)[a]
East bank	h	Plant remains (*Liliopsida*)	2365 ± 35	2410 ± 80
-	f	Organic sediment	2560 ± 40	2720 ± 40
-	e	Organic sediment	2485 ± 30	2590 ± 130
-	d	Organic sediment	2455 ± 35	2455 ± 95
-	b	Organic sediment (*Liliopsida*)	2850 ± 40	2965 ± 110
West bank	a	Charcoal (*Pinopsida*)	5270 ± 40	6030 ± 100
-	b	Sed + small plant remains (*Pinopsida*)	6690 ± 60	7560 ± 100

[a]Calendar ages at 2σ, calibrated using CALIB 7.0.4 based on IntCal13 curve [*Reimer et al*., 2013]. Altitude of Site 1: 3737 m.

depth, respectively [*Zhou et al*., 2002]. In order to compare the peat age of our site with the *Zhou et al*. [2002] peat ages and to provide an age bound to our alluvial fan, we sampled the peat deposits (on the east bank of the river only). We sampled the soil at 5 levels: 135, 150, 170, 180, and 225 cm depth (Figures 8d and 8e). Radiocarbon analyses yield ages of 2410 ± 80, 2720 ± 40, 2590 ± 130, 2455 ± 95, and 2965 ± 110 cal yr B.P., respectively (Table 2). We notice that ages are not correlated with depth (Figure 8e), which is probably related to some sediment reworking during deposition condition changes. However, the scatter between ages is negligible as the age mean deviation is 172 ± 25 cal yr B.P., so the mean age of the peat deposit can be estimated around ~2630 ± 90 cal yr B.P., which is consistent with the Hongyuan peat ages from *Zhou et al*. [2002]. Ages derived from the upper part of the alluvial fan and the soil are thus significantly different, with a time gap of more than 4000 years between the two deposits. This time interval suggests either that the top of the alluvial fan has been eroded, and then covered by a soil, or that during 4000 years the fan was inactive at this location. In the first case, the minimum fan age (6795 ± 100 cal yr B.P.) could be even younger.

To derived a slip rate, we assume that the alluvial fan (F1) and the river that entrenches it starts to record and accumulate displacements when the fan ends to form, such that derived organic material ages from the upper part of the alluvial fan can approximately be related to the age of the largest displacement. Considering the largest displacement, at the alluvial fan scale, of 23.0 ± 7.0 m (Figure 7c′), recorded by the offset river and the mean (minimum) age of the fan is 6795 ± 100 cal yr B.P., we estimate a dextral slip rate for the Longriqu fault of 3.4 ± 1.1 mm yr^{-1} (averaged through the Holocene). As the alluvial fan age has been derived from near fan surface samples, we can consider that the inferred slip rate likely corresponds to a maximum slip rate.

4.4. Site 2 (32°41.313′N, 102°42.645′E)

4.4.1. Site Presentation

Site 2 is located less than 5 km west of Site 1 on segment S4a (Figure 3c). The site is easily accessible owing to a road located 300 m east of it that crosses the Longriqu fault. The site corresponds to an alluvial fan ~370 m long and ~160 m wide covered by peat and vegetation. We sampled at two locations: Site 2a located less than 10 m north the Longriqu fault and Site 2b at 20 m south the fault (Figure 9a). Site 2 records two offsets of 7.6 ± 1.9 and 40.0 ± 5.0 m (Figures 9b–9c′). The smallest offset has been measured by realigning the current major river, which carves into the alluvial fan, and a smaller channel located west of this river (bb′, dd′, Figure 9c). On the eastern side of the fan, a former channel, presently filled by wet peat deposits (marsh), has been offset by 40.0 ± 5.0 m (cc′, Figures 9b and 9c′). The westernmost small channel observed only downstream the fault (a′ (=d′), Figures 9b and 9c′), also seems to have been displaced by it. We interpret this channel as formerly connected to the present-day upstream part of the river (upstream of the fault), then displaced by ~40 m (aa′, Figure 9c′) and finally captured, leading to the present-day morphology (Figure 9b). No terrace riser can be clearly identified in the alluvial fan, but we can distinguish the alluvial fan surface (F1) and the current river bed deposit (T0) (Figures 10a and 10b). Samples from Site 2 were collected along two vertical profiles from both sides of the present-day river, upstream and downstream of the fault (Figure 10b). On the east bank (Site 2a, upstream of the fault), we collected seven samples every 40 cm from 10 to 110 cm depth (Figure 10c), and on the west bank (Site 2b, downstream of the fault) we collected nine samples from 5 to 200 cm depth (Figure 10d). Samples are essentially pebbles of quartz and schist (Table 3).

4.4.2. Alluvial Fan Age

To determine the exposure time of the alluvial fan, we measured the concentration of in situ produced ^{10}Be that accumulates through time in quartz-rich pebbles exposed to cosmic rays [e.g., *Lal*, 1991; Gosse and Phillips, 2001]. Collected pebbles were crushed and sieved to extract the 250–1000 μm fraction. After

Table 3. ^{10}Be Analytical Results[a]

Sample	Pebble Material	Depth (m)	[^{10}Be] (at. g^{-1})	[^{10}Be] Error (at. g^{-1})
S2a10	Quartz pebbles	10	618188	19506
S2a30	Quartz, schist	30	2161234	11788
S2a50	Quartz, schist	50	137382	6313
S2a70	Quartz, schist	70	137945	6983
S2a90	Quartz, schist	90	158199	7277
S2a110	Quartz, schist	110	133701	7216
S2b5	Quartz, schist	5	431478	13606
S2b40	Quartz, schist	40	488171	15706
S2b60	Quartz, schist	60	102299	3443
S2b80	Quartz, schist	80	64824	2323
S2b120	Quartz, schist	120	54676	2088
S2b140	Quartz pebbles	140	49226	1807
S2b140	Quartz, schist	140	46701	1735
S2b160	Quartz, schist	160	65418	2313
S2b200	Quartz, schist	200	26937	1227

[a]Longitude: 102 42.647. Latitude: 32 41.302. Altitude: 3676 m.

magnetic separation, the nonmagnetic fraction was etched in one third HCl and two thirds H_2SiF_6 until pure quartz was obtained. Three additional HF leachings were used to remove atmospheric ^{10}Be absorbed on quartz grains. The samples were spiked with 100 μL of an in-house ^{9}Be carrier solution ($3.03.10^{-3}$ g·g^{-1}) before total digestion [*Merchel et al*., 2008]. Beryllium was finally extracted using standard ion exchange columns and oxidized into BeO. The ^{10}Be/^{9}Be ratios were measured at the French accelerator mass spectrometry (AMS) ASTER facility in Aix-en-Provence [*Arnold et al*., 2010, 2013]. The obtained ^{10}Be/^{9}Be ratios were corrected for procedural blanks and calibrated against the National Institute of Standards and Technology standard reference material 4325 by using an assigned value of $2.79 \pm 0.03 \times 10^{-11}$ [*Nishiizumi et al*., 2007]. Analytical uncertainties (reported as 1σ) include uncertainties associated with AMS counting statistics, chemical blank measurements, and AMS internal error (0.5%). A sea level, high-latitude (SLHL) spallation production of 4.03 ± 0.18 at g^{-1} yr^{-1} was used and scaled for latitude [*Stone*, 2000] and elevation [*Lal*, 1991]. The in situ ^{10}Be concentration is time and depth dependent, such that ^{10}Be concentration depth profile should follow an exponential decrease [*Lal*, 1991]. If this is the case, both the erosion rate and surface exposure time can be constrained [*Siame et al*., 2004]. Surface exposure (or abandonment) ages were calculated using estimates of the nuclear particles contribution proposed by *Braucher et al*. [2011] and modeled using a χ^2 inversion method proposed by *Siame et al*. [2004].

The ^{10}Be concentration evolution at depth in both vertical profiles display exponential decrease (Figures 11a and 11b). However, both also show that the shallowest samples are strikingly enriched in ^{10}Be, suggesting two different stages of deposition. The best-fitting model for both Sites 2a and 2b, taking into account all samples, imply a density Rho > 5 g cm^{-3}, which is definitely not realistic (Figures 11a and 11b). If we use a more reasonable 2.1 g cm^{-3} alluvial fan density and remove the samples from the soil, both sites present ^{10}Be concentration depth profile in steady state, such that only a minimum exposure time can be derived (Figures 11c and 11d). Although the model fits well the data and the derived erosion rate is acceptable compared to denudation rates measured in the area (between 0.04 and 0.1 mm yr^{-1} [*Ansberque et al*., 2015]), the neutrons absorption length given by the fit regression considering all data, of 102 g cm^{-2} for Site 2a and of 117 g cm^{-2} for Site 2b, are too low (Figures 11c and 11d); the minimum absorption length of combined neutrons and muons should be ≥160 g cm^{-2}. Removing the soil, ^{10}Be-rich samples yields acceptable absorption length (~210 g cm^{-2}) (Figures 11c and 11d), which suggests that to keep a correct absorption length, with all of the samples, several centimeters of surface erosion is required. Trying to reconcile all the above mentioned conditions for Site 2a, using an erosion rate given by the sample at the surface (0.05 mm yr^{-1}), the samples must have been 70 cm deeper (Figure 11e). Considering a soil removal of 70 cm, the age of the fan cannot be assessed as the profile has reached a steady state, but a minimum exposure time of 15.6 ka can be estimated. As the Site 2b presents the same characteristics than Site 2a, we followed the same steps of calculations to derive its minimum exposure time and obtain a minimum exposure time of 10.8 ka with 84 cm of surface removal and an erosion rate of 0.07 mm yr^{-1} (Figure 11f).

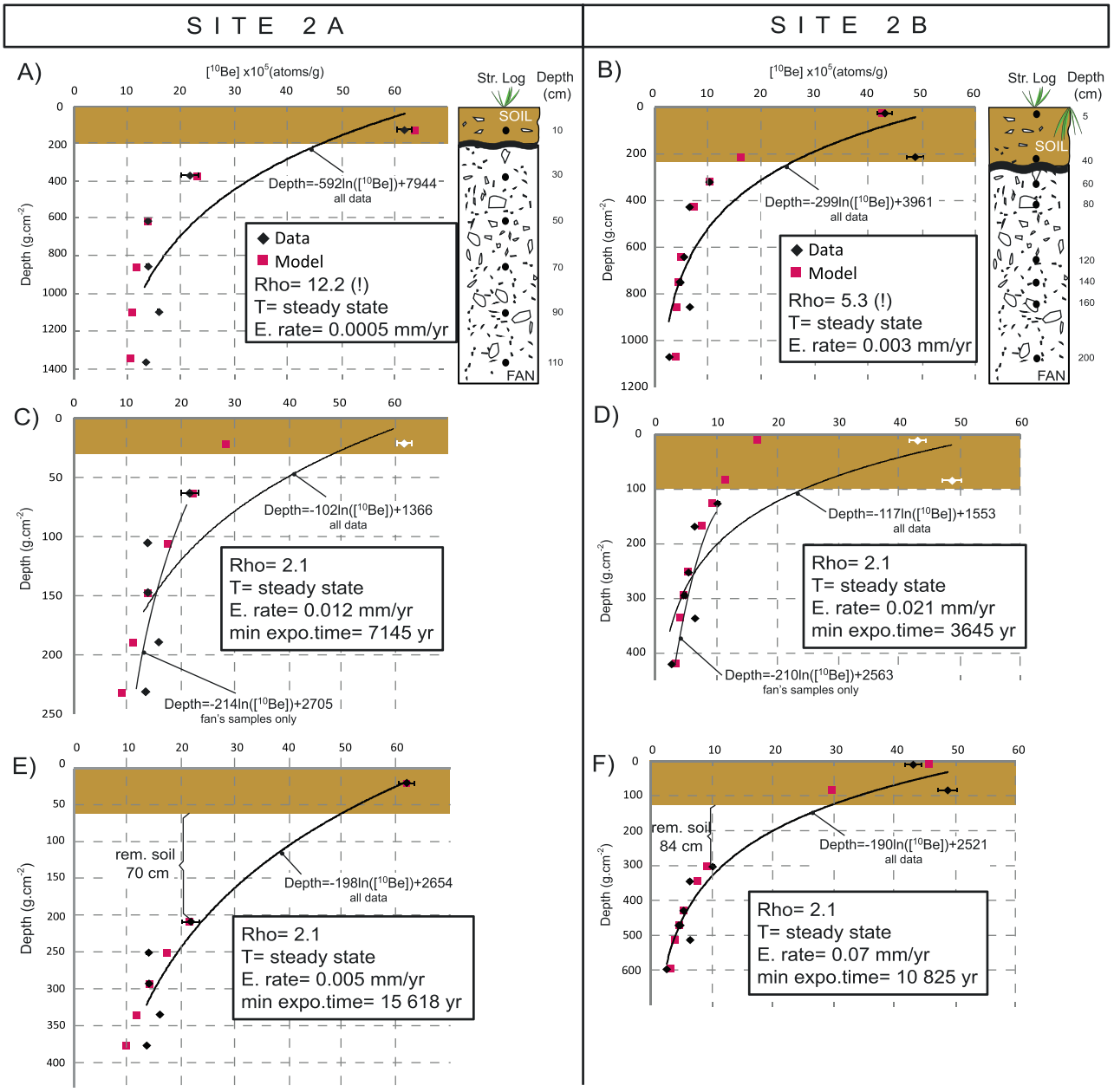

Figure 11. (a and b) Depth-^{10}Be concentration profiles of Sites 2a and 2b, respectively. (c and d) Depth-^{10}Be concentration profiles without soil samples for both sites (white dots). (e and f) Depth-^{10}Be concentration profiles considering that samples should be 70 cm (Site 2a) and 84 cm (Site 2b) deeper with respect to the fan surface than their present-day depth (rem. soil: removed soil). Black lines are logarithmic regressions through the data. Depth axis is density-dependent converted into g cm^{-2}.

The deepening of the samples for profile modeling (Figures 11e and 11f) can be explained by a partial dissolution of the top of the fan followed by the development of a soil, which build up using the most weathering-resistant fan materials, such as quartz pebbles. Such processes have been described by *Molliex et al.* [2013] to explain the ^{10}Be concentration discrepancy between samples at fan or terrace surface and deeper samples. Sites 2a and 2b do not form distinct terraces or levels, we thus average their minimum exposure ages to 13.2 ± 2.4 ka.

4.4.3. Dextral Slip Rate Estimate

To calculate a dextral slip rate based on offset measurements and the ^{10}Be dating method, we assume that the alluvial fan starts to record and accumulate displacements once it ends to significantly develop so that

the exposure (or abandoned) time of the alluvial fan surface can be related to the age of the largest displacement it records. Considering the largest displacement of 40.0 ± 5.0 m and the mean (minimum) alluvial fan age of 13.2 ± 2.4 ka, we calculate a slip rate of 3.0 ± 1.1 mm yr^{-1}. As the alluvial fan age corresponds to the minimum exposure time, we can consider that the inferred slip rate corresponds to a maximum estimate close to the true slip rate.

5. Discussion

5.1. Slip Rate Over the Holocene

The dextral slip rates that were estimated using two displaced alluvial fans dated with two different dating methods are strongly consistent: the maximum dextral slip rate estimated from Site 1 is 3.4 ± 1.1 mm yr^{-1} (since ~7 ka) and 3.0 ± 1.1 mm yr^{-1} from Site 2 (since ~13 ka). The mean (maximum) dextral slip rate of the Longriqu fault is thus estimated at 3.2 ± 1.1 mm yr^{-1}. However, the two studied sites suggest that the top of the fans has been eroded or weathered. Then the derived age may not represent the minimum age of the fan, and the dextral slip rate on the Longriqu fault is maybe slightly underestimated. *Ren et al*. [2013b] estimated a dextral slip rate on the Longriqu fault ranging from ~1.4 to 2.5 mm yr^{-1} averaged over ~18 ka, which is lower than our dextral slip rate estimate from 7 to 13 ka. This difference may be explained by considering the *Ren et al*. [2013b] sites location along segment S1b (likely interacting with S2a) nearby the beginning of the main restraining bend between S1 and S2 (Figure 3c). Indeed, at the tip of a discontinuity, slip rate can decrease, as part of slip along a restraining bend is converted into vertical motion [e.g., *Peacock*, 1991; *Bürgmann et al*., 2006]. The vertical motion estimated by *Ren et al*. [2013b] at their site locations is 0.1 ± 0.1 mm yr^{-1} (since 11 ka).

Multiple studies have reported and discussed discrepancies between geodetically determined slip rates and those inferred from reconstruction of displaced and dated fluvial markers [e.g., *Cowgill*, 2007; *Meade et al*., 2013]. Over geodetic timescale, the dextral slip rate on the LFS is 5 ± 1 mm yr^{-1} [*Shen et al*., 2009]. As the LFS consists of two fault zones and as the Longriqu fault has a slightly faster dextral slip rate than the Maoergai fault [*Ren et al*., 2013b], the maximum 3.2 ± 1.1 mm yr^{-1} slip rate estimated for the Longriqu fault is consistent with present-day rates across the LFS and confirms that the system has an important role on the accommodation of the eastern Tibetan margin deformation.

5.2. Potential Earthquake Magnitude

Pleiades images allowed us to identified six major segments and at least 12 secondary segments, along an 80 km long portion of the Longriqu fault. The Longriqu fault geometry and geomorphology (large restraining bends and overlaps) display evidence for its maturity (Figure 3). Although, in details, secondary segments form small discontinuities, we presume that the Longriqu segments are connected to each other at the crustal scale. As connected segments may interact together during an earthquake, generated at seismogenic depths [*Wells and Coppersmith*, 1994], we cannot exclude a complete rupture of the whole studied 80 km long portion of the Longriqu fault in a single rupture. A rupture length of 80 km would produce a M_w 7.3–7.4 earthquake and a maximum coseismic displacement of ~3.5 m [*Wells and Coppersmith*, 1994]. The Longriqu fault accommodates ~0.1 mm yr^{-1} of reverse slip rate [*Ren et al*., 2013b]. The estimated 3.2 mm yr^{-1} strike-slip rate and the 0.1 mm yr^{-1} reverse slip rate would account respectively for ~100% and ~3% of the true slip vector of the Longriqu fault. Then even taking into account the reverse slip rate component, the estimated earthquake magnitude would not be much higher than 7.4.

Our Longriqu fault segmentation map covers only 80 km of the fault system, because farther west and east glacial erosion and modern deposits do not allow to observe the fault trace (Figure 1). However, we think that the present-day morphological signature of the LFS, which has preferentially developed south of the Ruoergai basin (Figure 2a), testifies of localized deformation along the fault system and that the LFS may have been reactivated first by a significant vertical motion in the past. Indeed, the positive relief and the basin, respectively, north and south the Longriqu fault, are unusual for a strike-slip fault-related topography and could be associated with a hangingwall and footwall (Figures 1 and 2). The location of this fault-related topography suggests that the deformation along the Longriqu fault is concentrated along the 80 km long studied zone. Likewise, the same assumption can be made for the Maoergai fault (Figures 1 and 2). If correct, as the

LFS is described as a ~300 km long system, the Longriqu and Maoergai faults could be composed of at least two regional-scale segments, with the most active one running into the studied area over 80 km.

5.3. Past Coseismic Displacements and Earthquake Recurrence

Long-term displacement patterns along the fault can be explained by different models, such as (i) the slip variable model, which predicts random earthquake size and variable along-fault displacement for each event [*Schwartz and Coppersmith*, 1984]; (ii) the uniform slip model, where large earthquakes generate periodically the same slip distribution along the same fault segment [*Sieh*, 1981]; and (iii) the characteristic earthquake model for which a single-event displacement at any point along the fault is constant from one earthquake to the other, resulting in a regular identical long-term slip pattern [*Schwartz and Coppersmith*, 1984]. To discriminate which model is relevant, the last rupture slip distribution along the fault and longer-term observations, such as cumulative displacements, are required. In our case, both are assessed from the PDF of offsets measurements (Figure 6).

Even though the fault segmentation map suggests that segments are connected at depth, each segment could behave independently through distinct earthquakes. This would lead to different PDF of the slip distribution for different segments. However, the PDFs from 0 to 22 km, and from 22 to 60 km along fault, display very similar offset ranges (Figures 6c and 6d). These results suggest that segments from S1 to S5 (Figure 6a) can rupture all together during earthquakes. The smallest offsets population observed on the PDF is 4.1 ± 0.9 m (Figure 6e). Following previous studies, we attribute this smallest offset range to the last earthquake. This ~4 m value is consistent with the 3.5 m maximum coseismic displacement deduced from scaling laws from *Wells and Coppersmith* [1994] (see section 6.2). We also assume that at least five earthquakes are well-preserved along the Longriqu fault, corresponding to the five well-distinct successive peaks (Figure 6e). In a characteristic slip model, each peak-to-peak wavelength corresponds to the coseismic characteristic displacement, and each peak value is a one-time increment of the coseismic slip value [*Zielke et al*., 2010, 2015; *Klinger et al*., 2011]. The peak-to-peak wavelength of our PDF is ~9 m, which is approximately twice the last earthquake displacement (Figure 6e). This suggests either that the slip distribution is not governed by a characteristic slip model or that only one event on two is well preserved. The first assumption would imply that the last earthquake generated a coseismic slip of ~4 m, while previous events generated ~9 m slip, which is not realistic regarding the 80 km potential rupture length. The second hypothesis would imply that the present-day PDF pattern reflects past climatic changes, which influence the preservation (peaks)/degradation (troughs) of displaced morphological markers. We favor this hypothesis, which has been explored in previous studies of alluvial surfaces offset by active faults over the Tibetan plateau [*van der Woerd et al*., 2002; *Meriaux et al*., 2012]. In fact, intermediate offset peaks are also observed in the PDF (for example, 8.1 m and 17.4 m, Figure 6e). Taking into account these peaks, we found a strikingly consistent, mean peak-to-peak wavelength of 4.3 ± 2.9 m over nine preserved earthquakes (Figure 6e).On the basis of our measured offsets distribution, we suggest that the Longriqu fault may follow a characteristic slip model with a ~4 m coseismic slip and a rupture length of ~80 km. Following the *Wallace* [1970] definition of the earthquake recurrence interval and according to our mean slip rate results and coseismic slip, we propose a time interval of $1340\ ^{+2085}_{-1020}$ years between earthquakes. This earthquake recurrence is consistent with the *Ren et al*. [2013a, 2013b] results, who calculated a ~1700 year recurrence interval.

5.4. Relationship Between Characteristic Slip Model and Regional Kinematic

Ren et al. [2013a, 2013b] distinguished several earthquakes on the Longriqu and Maoergai fault with at least one apparently rupturing the two faults simultaneously. As both fault zones belong to the same system, we could suggest that the Maoergai fault also follows a characteristic slip model. Such behavior is intimately related to how the LFS area and more broadly the eastern Tibetan Plateau deforms. *Caniven* [2014] showed that characteristic slip is favored where tectonic stress loading rate is slow and suggested that this slip model is the result of weak coupling between upper and lower crusts. Several kinematic models, which were proposed to explain the deformation mechanisms of eastern Tibet, suggest the presence of a décollement zone at the brittle/ductile transition on which the Longmen Shan structures and the LFS are rooted [e.g., *Hubbard et al*., 2010; *Ren et al*., 2013b]. Thus, the characteristic slip model we point out for the Longriqu fault in this study could be a consequence of a weak coupling between upper and lower crusts owing to the décollement.

6. Conclusion

In this paper, we used high-resolution Pleiades images that we combined with morphotectonic field survey to propose a detailed segmentation map, at kilometric to metric scale, along the 80 km long well-expressed section of the Longriqu fault. We identified six major segments and at least 12 secondary segments, which are arranged to form a mature fault segmentation. The inventory of displacements along the Longriqu fault shows that at least five segments can rupture simultaneously, suggesting that the whole 80 km long studied zone can rupture and produce 7.3−7.4 magnitude earthquakes. The slip distribution allows to propose a ~4 m coseismic slip and to suggest that nine earthquakes are geomorphologically preserved along the fault. We estimated a late Quaternary maximum dextral slip rate of 3.2 ± 1.1 mm yr^{-1}, inferred from displaced and dated alluvial fans (with ^{14}C and ^{10}Be methods), and then an earthquake recurrence of ~1300 years. Finally, we suggest a characteristic slip model for the Longriqu fault, which bears with the idea of a weak coupling between the upper and lower crusts in that area.

Acknowledgments

This work is part of a PhD thesis by C. Ansberque (CEREGE-AMU, OSU Pytheas) funded by the French Ministry of Superior Education and Research. We thank the French National Research Agency (ANR) AA-PJCJC SIMI5-6 LONGRIBA and INSU-CNRS for financial support. We also thank all the master students of Xu Xiwei and Li Yong (from the China Earthquake Administration at Beijing and the Chengdu University of Technology at Chengdu) for their helpful contribution to our field work. Pleiades images were obtained through an ISIS project funded by the Centre National d'Etudes Spatiales (CNES). The French AMS national facility ASTER (CEREGE, Aix-en-Provence) is supported by the INSU/CNRS, ANR through the "Projets thématique d'excellence" Program for the "Equipements d'Excellence" ASTER-CEREGE action, IRD, and CEA. Data are available upon request at ansberque@cerege.fr. We also want to thank M. Rizza for her valuable remarks on offset measurements, A. Moulin and D. Barboni for sharing interesting discussion on the relation between earthquakes and climate changes, C. Keller and A. Alexandre for their explanation on peat formation, and J. Fleury and P. Dussouillez, who managed the ENVI software at CEREGE. Our final thanks go to Mark Allen and an anonymous reviewer, and to the Associate Editor Djordje Grujic for their constructive reviews.

References

Aki, K. (1984), Asperities, barriers, characteristic earthquakes and strong motion prediction, *J. Geophys. Res.*, *89*(B7), 5867–5872, doi:10.1029/JB089iB07p05867.

Ansberque, C., V. Godard, O. Bellier, J. De Sigoyer, J. Liu-Zeng, X. Xu, Z. Ren, Y. Li, and A. S. T. E. R. Team (2015), Denudation pattern across the Longriba fault system and implications for the geomorphological evolution of the eastern Tibetan margin, *Geomorphology*, *246*, 542–557, doi:10.1016/j.geomorph.2015.07.017.

Arnold, M., S. Merchel, D. L. Bourlès, R. Braucher, L. Benedetti, R. C. Finkel, G. Aumaître, A. Gottdang, and M. Klein (2010), The French accelerator mass spectrometry facility ASTER: Improved performance and developments, *Nucl. Instrum. Methods Phys. Res., Sect. B*, *268*(11–12), 1954–1959, doi:10.1016/j.nimb.2010.02.107.

Arnold, M., G. Aumaître, D. L. Bourlès, K. Keddadouche, R. Braucher, R. C. Finkel, E. Nottoli, L. Benedetti, and S. Merchel (2013), The French accelerator mass spectrometry facility ASTER after 4 years: Status and recent developments on 36Cl and 129I, *Nucl. Instrum. Methods Phys. Res., Sect. B*, *294*, 24–28, doi:10.1016/j.nimb.2012.01.049.

Arrowsmith, J. R., and O. Zielke (2009), Tectonic geomorphology of the San Andreas Fault zone from high resolution topography: An example from the Cholame segment, *Geomorphology*, *113*(1–2), 70–81, doi:10.1016/j.geomorph.2009.01.002.

Barka, A. (1996), Slip distribution along the North Anatolian fault associated with the large earthquakes of the period 1939 to 1967, *Bull. Seismol. Soc. Am.*, *86*(5), 1238–1254.

Barka, A. A., and E. Kadinsky-Cade (1988), Strike-slip fault geometry in Turkey and its influence on earthquake activity, *Tectonics*, *7*(3), 663–684, doi:10.1029/TC007i003p00663.

Bellier, O., M. Sébrier, S. Pramumijoyo, T. Beaudouin, H. Harjono, I. Bahar, and O. Forni (1997), Paleoseismicity and seismic hazard along the Great Sumatran Fault (Indonesia), *J. Geodyn.*, *24*, 169–183, doi:10.1016/S0264-3707(96)00051-8.

Bellier, O., M. Sébrier, T. Beaudoin, M. Villeneuve, R. Braucher, D. Bourlès, L. Siame, E. Putranto, and I. Pratomo (2001), High slip rate for a low seismicity along the Palu-Kolo active fault in central Sulawesi (Indonesia), *Terra Nova*, *13*, 463–470.

Braucher, R., S. Merchel, J. Borgomano, and D. L. Bourlès (2011), Production of cosmogenic radionuclides at great depth: A multi element approach, *Earth Planet. Sci. Lett.*, *309*, 1–9, doi:10.1016/j.epsl.2011.06.036.

Bürgmann, R., G. Hilley, A. Ferretti, and F. Novali (2006), Resolving vertical tectonics in the San Francisco Bay Area from permanent scatterer InSAR and GPS analysis, *Geology*, *34*(3), 221–224, doi:10.1130/G22064.1.

Caniven, Y. (2014), Cinématique et mécanique des failles décrochantes à l'échelle de temps du cycle sismique: Apports d'un modèle expérimental (kinematics and mechanics of strike-slip faults at the seismic cycle timescale: insights from experimental models), PhD thesis, Montpellier 2 Univ.

Chen, F. H., J. Bloemendal, P. Z. Zhang, and G. X. Liu (1999), An 800 ky proxy record of climate from lake sediments of the Zoige Basin, eastern Tibetan Plateau, *Palaeogeogr. Palaeoclimatol. Palaeoecol.*, *151*, 307–320.

Cowgill, E. (2007), Impact of riser reconstructions on estimation of secular variation in rates of strike–slip faulting: Revisiting the Cherchen River site along the Altyn Tagh Fault, NW China, *Earth Planet. Sci. Lett.*, *254*(3–4), 239–255, doi:10.1016/j.epsl.2006.09.015.

Dominguez, S., J. P. Avouac, and R. Michel (2003), Horizontal coseismic deformation of the 1999 Chi-Chi earthquake measured from SPOT satellite images: Implications for the seismic cycle along the western foothills of central Taiwan, *J. Geophys. Res.*, *108*(B2), 2156–2202, doi:10.1029/2001JB000951.

Fu, B., Y. Ninomiya, X. Lei, S. Toda, and Y. Awata (2004), Mapping active fault associated with the 2003 M_w 6.6 Bam (SE Iran) earthquake with ASTER 3D images, *Remote Sens. Environ.*, *92*(2), 153–157, doi:10.1016/j.rse.2004.05.019.

Gaudemer, Y., P. Tapponnier, and D. L. Turcotte (1989), River offsets across active strike-slip faults, *Ann. Tect.*, *III*(2), 55–79.

Godard, V., and D. W. Burbank (2011), Mechanical analysis of controls on strain partitioning in the Himalayas of central Nepal, *J. Geophys. Res.*, *116*, B10402, doi:10.1029/2011JB008272.

Gold, P. O., M. E. Oskin, A. J. Elliott, A. Hinojosa-Corona, M. H. Taylor, O. Kreylos, and E. S. Cowgill (2013), Coseismic slip variation assessed from terrestrial lidar scans of the El Mayor-Cucapah surface rupture, *Earth Planet. Sci. Lett.*, *366*(3013), 151–162, doi:10.1016/j.epsl.2013.01.040.

Gosse, J. C., and F. M. Phillips (2001), Terrestrial in situ cosmogenic nuclides: theory and application, *Quat. Sci. Rev.*, *20*, 1475–1560.

Grant Ludwig, L., S. O. Akçiz, G. R. Noriega, O. Zielke, and J. R. Arrowsmith (2010), Climate-modulated channel incision and rupture history of the San Andreas Fault in the Carrizo Plain, *Science*, *327*, 1117–1119, doi:10.1126/science.1182837.

Guo, C. X., F. Luo, X. Ding, Q. Luo, C. X. Luo, Y. Cai, J. Zhao, S. Feng, Z. R. Yang, and J. Zhang (2013), Palaeoclimate reconstruction based on pollen records from the Tangke and Riganqiao peat sections in the Zoige Plateau, China, *Quat. Int.*, *286*, 19–28, doi:10.1016/j.quaint.2012.09.027.

Guo, X., R. Gao, G. R. Keller, X. Xu, H. Wang, and W. Li (2013), Imaging the crustal structure beneath the eastern Tibetan Plateau and implications for the uplift of the Longmen Shan, *Earth Planet. Sci. Lett.*, *379*, 72–80, doi:10.1016/j.epsl.2013.08.005.

Guo, X., R. Gao, X. Xu, G. R. Keller, A. Yin, and X. Xiong (2015), Longriba fault zone in eastern Tibet: An important tectonic boundary marking the westernmost edge of the Yangtze block, *Tectonics*, *34*, 970–985, doi:10.1002/2015TC003880.

Harkins, N., E. Kirby, A. Heimsath, R. Robinson, and U. Reiser (2007), Transient fluvial incision in the headwaters of the Yellow River, northeastern Tibet, China, *J. Geophys. Res.*, *112*, 1–21, doi:10.1029/2006JF000570.

Harkins, N., E. Kirby, X. Shi, E. Wang, D. W. Burbank, and F. Chun (2010), Millenial slip rates along the eastern Kunlun fault: Implications for the dynamics of intracontinental deformation in Asia, *Lithosphere*, *2*(4), 247–266, doi:10.1130/L85.1.

Harrowfield, M. J., and C. J. L. Wilson (2005), Indosinian deformation of the Songpan Garzê Fold Belt, northeast Tibetan Plateau, *J. Struct. Geol.*, *27*, 101–117.

Heki, K. (2001), Seasonal modulation of interseismic strain buildup in northeastern Japan driven by snow loads, *Science*, *293*(5527), 89–92, doi:10.1126/science.1061056.

Hetzel, R., and A. Hampel (2005), Slip rate variations on normal faults during glacial-interglacial changes in surface loads, *Nature*, *435*(7038), 81–84, doi:10.1038/nature03562.

Hetzel, R., and A. Hampel (2006), Long-term rates of faulting derived from cosmogenic nuclides and short-term variations caused by glacial-interglacial volume changes of glaciers and lakes, *Int. J. Modern Phys. B*, *20*(03), 261–276, doi:10.1142/S0217979206033255.

Hubbard, J., J. H. Shaw, and Y. Klinger (2010), Structural setting of the 2008 M_w 7.9 Wenchuan China, Earthquake, *Bull. Seismol. Soc. Am.*, *100*(5B), 2713–2735, doi:10.1785/0120090341.

Jia, S. X., X. K. Zhang, J. R. Zhao, F. Y. Wang, C. K. Zhang, Z. F. Xu, J. Pan, Z. Liu, S. Pan, and G. W. Sun (2010), Deep seismic sounding data reveal the crustal structures beneath Zoige basin and its surrounding folded orogenic belts, *Sci. China Earth Sci.*, *53*(2), 203–212, doi:10.1007/s11430-009-0166-0.

Klinger, Y., X. Xu, P. Tapponnier, J. Van der Woerd, C. Lasserre, and G. King (2005), High-resolution satellite imagery mapping for the surface rupture and slip distribution of the M_w ~ 7.8, 14 November 2001 Kokoxili earthquake, Kunlun fault, northern Tibet, China, *Bull. Seismol. Soc. Am.*, *95*(5), 1970–1987, doi:10.1785/0120040233.

Klinger, Y., M. Etchebes, P. Tapponnier, and C. Narteau (2011), Characteristic slip for five great earthquakes along the Fuyun fault in China, *Nat. Geosci.*, *4*(6), 389–392, doi:10.1038/ngeo1158.

Lal, D. (1991), Cosmic ray labeling of erosion surfaces: In situ nuclide production rates and erosion models, *Earth Planet. Sci. Lett.*, *104*, 424–439.

Li, J.-J., et al. (1997), Magnetostratigraphic dating of river terraces: Rapid and intermittent incision by the Yellow River of the northeastern margin of the Tibetan Plateau during the Quaternary, *J. Geophys. Res.*, *102*, 10,121–10,132, doi:10.1029/97JB00275.

Manighetti, I., M. Campillo, C. Sammis, P. M. Mai, and G. King (2005), Evidence for self-similar, triangular slip distributions on earthquakes: Implications for earthquake and fault mechanics, *J. Geophys. Res.*, *110*, B05302, doi:10.1029/2004JB003174.

Manighetti, I., C. Caulet, D. De Barros, C. Perrin, F. Cappa, and Y. Gaudemer (2015), Generic along-strike segmentation of Afar normal faults, East Africa: Implications on fault growth and stress heterogeneity on seismogenic fault planes, *Geochem. Geophys. Geosyst.*, *16*, 443–467, doi:10.1002/2014GC005691.

Mattauer, M., J. Malavieille, D. Calassou, J. Lancelot, F. Roger, Z. Hao, Z. Xu, and L. Hou (1992), La chaîne triassique de Songpan Ganze (Ouest Sechuan et Est Tibet); une chaîne de plissement-décollement sur marge passive, *C. R. Acad. Sci., Paris*, *314*(6), 619–626.

McGill, S. F., and K. Sieh (1991), Surficial offsets on the Central and Eastern Garlock Fault associated with prehistoric earthquakes, *J. Geophys. Res.*, *96*(B13), 597–621, doi:10.1029/91JB02030.

Meade, B. J., Y. Klinger, and E. A. Hetland (2013), Inference of multiple earthquake-cycle relaxation timescales from irregular geodetic sampling of interseismic deformation, *Bull. Seismol. Soc. Am.*, *103*(5), 2824–2835, doi:10.1785/0120130006.

Merchel, S., M. Arnold, G. Aumaître, L. Benedetti, D. L. Bourlès, R. Braucher, V. Alfimov, S. P. H. T. Freeman, P. Steier, and A. Wallner (2008), Towards more precise 10Be and 36Cl data from measurements at the 10^{-14} level: Influence of sample preparation, *Nucl. Instrum. Methods Phys. Res., Sect. B*, *266*, 4921–4926, doi:10.1016/j.nimb.2008.07.031.

Meriaux, A.-S., J. van der Woerd, P. Tapponnier, F. J. Ryerson, R. C. Finkel, C. Lasserre, and X. Xu (2012), The Pingding segment of the Altyn Tagh Fault (91°E): Holocene slip-rate determination from cosmogenic radionuclide dating of offset fluvial terraces, *J. Geophys. Res.*, *117*, B09406, doi:10.1029/2012JB009289.

Métivier, F., Y. Gaudemer, P. Tapponnier, and B. Meyer (1998), Northeastward growth of the Tibet Plateau deduced from balanced reconstruction of two depositional areas: The Qaidam and Hexi Corridor basins, China, *Tectonics*, *17*, 823–842, doi:10.1029/98TC02764.

Mischke, S., and C. Zhang (2010), Holocene cold events on the Tibetan Plateau, *Global Planet. Change*, *72*(3), 155–163, doi:10.1016/j.gloplacha.2010.02.001.

Molliex, S., L. L. Siame, D. L. Bourlès, O. Bellier, R. Braucher, and G. Clauzon (2013), Quaternary evolution of a large alluvial fan in a periglacial setting (Crau Plain, SE France) constrained by terrestrial cosmogenic nuclide (10Be), *Geomorphology*, *95*, 45–52, doi:10.1016/j.geomorph.2013.04.025.

Molnar, P., and P. Tapponnier (1977), Relation of the tectonics of eastern China to the India-Eurasia collision: Application of slip-line field theory to large-scale continental tectonics, *Geology*, *5*, 212–216, doi:10.1130/0091-7613(1977)5<212:ROTTOE>2.0.CO;2.

Nishiizumi, K., M. Imamura, M. W. Caffee, J. R. Southon, R. C. Finkel, and J. McAninch (2007), Absolute calibration of 10Be AMS standards, *Nucl. Instrum. Methods Phys. Res., Sect. B*, *258*(2), 403–413, doi:10.1016/j.nimb.2007.01.297.

Peacock, D. C. P. (1991), Displacements and segment linkage in strike-slip fault zones, *J. Struct. Geol.*, *13*(9), 1025–1035, doi:10.1016/0191-8141(91)90054-M.

Pullen, A., P. Kapp, G. E. Gehrels, J. D. Vervoort, and L. Ding (2008), Triassic continental subduction in central Tibet and Mediterranean-style closure of the Paleo-Tethys Ocean, *Geology*, *36*(5), 351–354, doi:10.1130/G24435A.1.

Reimer, P., et al. (2013), INTCAL09 and MARINE09 radiocarbon age curves, 0–50,000 years cal BP, *Radiocarbon*, *51*(4), 1111–1150, doi:10.2458/azu_js_rc.55.16947.

Ren, J., X. Xu, R. S. Yeats, S. Zhang, R. Ding, and Z. Gong (2013a), Holocene paleoearthquakes of the Maoergai fault, eastern Tibet, *Tectonophysics*, *590*, 121–135, doi:10.1016/j.tecto.2013.01.017.

Ren, J., X. Xu, R. S. Yeats, and S. Zhang (2013b), Latest Quaternary paleoseismology and slip rates of the Longriba fault zone, eastern Tibet: Implications for fault behavior and strain partitioning, *Tectonics*, *32*, 216–238, doi:10.1002/tect.20029.

Ren, Z., Z. Zhang, T. Chen, S. Yan, J. Yin, P. Zhang, W. Zheng, H. Zhang, and C. Li (2015), Clustering of offsets on the Haiyuan fault and their relationship to paleoearthquakes, *Geol. Soc. Am. Bull.*, doi:10.1130/B31155.1.

Ritz, J. F., E. T. Brown, D. L. Bourlès, H. Philip, A. Schlupp, G. M. Raisbeck, F. Yiou, and B. Enkhtuvshin (1995), Slip rates along active faults estimated with cosmic-ray–exposure dates: Application to the Bogd fault, Gobi-Altaï, Mongolia, *Geology*, *3*(11), 1019–1022, doi:10.1130/0091-7613(1995),023<1019:SRAAFE>,2.3.CO;2.

Roger, F., J. Malavieille, P. H. Leloup, S. Calassou, and Z. Xu (2004), Timing of granite emplacement and cooling in the Songpan–Garzê Fold Belt (eastern Tibetan Plateau) with tectonic implications, *J. Asian Earth Sci.*, *22*, 465–481, doi:10.1016/S1367-9120(03)00089-0.

Roger, F., M. Jolivet, and J. Malavieille (2008), Tectonic evolution of the Triassic fold belts of Tibet, *C. R. Geosci.*, *340*, 180–189, doi:10.1016/j.crte.2007.10.014.

Roger, F., M. Jolivet, and J. Malavieille (2010), The tectonic evolution of the Songpan-Garzê (North Tibet) and adjacent areas from Proterozoic to present: A synthesis, *J. Asian Earth Sci.*, *39*, 254–269, doi:10.1016/j.jseaes.2010.03.008.

Schwartz, D. P., and K. J. Coppersmith (1984), Fault behavior and characteristic earthquakes: Examples from the Wasatch and San Andreas Fault Zones, *J. Geophys. Res.*, *89*(B7), 5681–5698, doi:10.1029/JB089iB07p05681.
Sengör, A. M. C. (1985), East Asian tectonic collage, *Nature*, *318*, 15–17.
Shen, Z. K., J. Sun, P. Zhang, Y. Wan, M. Wang, R. Bürgmann, Y. Zeng, W. Gan, H. Liao, and Q. Wang (2009), Slip maxima at fault junctions and rupturing of barriers during the 2008 Wenchuan earthquake, *Nat. Geosci.*, *2*(10), 718–724, doi:10.1038/ngeo636.
Siame, L., M. Sébrier, O. Bellier, D. L. Bourlès, J. C. Castano, M. Aurojo, F. Yiou, and G. M. Raisbeck (1996), Segmentation and horizontal slip-rate estimation of the El Tigre fault zone, San Juan province (Argentina) from SPOT images analysis. Third ISAG, St Malo (France), 17-19/9/1996.
Siame, L., et al. (2004), Local erosion rates versus active tectonics: Cosmic ray exposure modelling in Provence (south-east France), *Earth Planet. Sci. Lett.*, *220*(3–4), 345–364, doi:10.1016/S0012-821X(04)00061-5.
Sibson, R. H. (1989), Earthquake faulting as a structural process, *J. Struct. Geol.*, *11*(1–2), 1–14, doi:10.1016/0191-8141(89)90032-1.
Sieh, K. E. (1981), A review of geological evidence for recurrence times of large earthquakes, in *Earthquake Prediction*, edited by D. W. Simpson and P. G. Richards, AGU, Washington, D. C., doi:10.1029/ME004p0181.
Sieh, K. E., and R. H. Jahns (1984), Holocene activity of the San Andreas fault at Wallace Creek, California, *Geol. Soc. Am. Bull.*, *95*(8), 883–896, doi:10.1130/0016-7606(1984)95<883:HAOTSA>2.0.CO;2.
Steer, P., M. Simoes, R. Cattin, J. Bruce, and H. Shyu (2014), Erosion influences the seismicity of active thrust faults, *Nat. Commun.*, *5*(5564), doi:10.1038/ncomms6564.
Stone, J. O. (2000), Air pressure and cosmogenic isotope production, *J. Geophys. Res.*, *105*(B10), 23,753–23,759, doi:10.1029/2000JB900181.
Thompson, T. B., A. Plesch, J. H. Shaw, and B. J. Meade (2015), Rapid slip-deficit rates at the eastern margin of the Tibetan Plateau prior to the 2008 M_w 7.9 Wenchuan earthquake, *Geophys. Res. Lett.*, *42*, 1677–1684, doi:10.1002/2014GL062833.
Tian, Y., B. P. Kohn, A. J. W. Gleadow, and S. Hu (2013), Constructing the Longmen Shan eastern Tibetan Plateau margin: Insights from low-temperature thermochronology, *Tectonics*, *32*(3), 576–592, doi:10.1002/tect.20043.
Van Der Woerd, J., P. Tapponnier, F. J. Ryerson, A. Meriaux, B. Meyer, Y. Gaudemer, R. C. Finkel, M. W. Caffee, G. Zhao, and Z. Xu (2002), Uniform postglacial slip-rate along the central 600 km of the Kunlun Fault (Tibet), from 26Al, 10Be, and 14C dating of riser offsets, and climatic origin of the regional morphology, *Geophys. J. Int.*, *148*, 356–388.
Wallace, R. E. (1968), Notes on stream channels offset by the San Andreas Fault, Southern Coast Ranges, California. Conference on Geologic Problems of the San Andreas Fault System.
Wallace, R. E. (1970), Earthquakes recurrence interval on the San Andreas Fault, *Geol. Soc. Am. Bull.*, *81*(10), 2875–2890, doi:10.1130/0016-7606(1970)81[2875:ERIOTS]2.0.CO;2.
Walsh, J. J., and J. Watterson (1988), Analysis of the relationship between displacements and dimensions of faults, *J. Struct. Geol.*, *10*(3), 239–247, doi:10.1016/0191-8141(88)90057-0.
Wang, E., E. Kirby, K. P. Furlong, M. van Soest, G. Xu, X. Shi, P. J. J. Kamp, and K. V. Hodges (2012), Two-phase growth of high topography in eastern Tibet during the Cenozoic, *Nat. Geosci.*, *5*, 640–645, doi:10.1038/ngeo1538.
Wells, D. L., and K. J. Coppersmith (1994), New empirical relationships among magnitude, rupture length, rupture width, rupture area, and surface displacement, *Bull. Seismol. Soc. Am.*, *84*(4), 974–1002.
Wesnousky, S. G. (2008), Displacement and geometrical characteristics of earthquake surface ruptures: Issues and implications for seismic-hazard analysis and the process of earthquake rupture, *Bull. Seismol. Soc. Am.*, *98*(4), 1609–1632, doi:10.1785/0120070111.
Xu, X., X. Wen, G. Chen, and G. Yu (2008), Discovery of the Longriba fault zone in eastern Bayan Har block, China and its tectonic implication, *Sci. China, Ser. D: Earth Sci.*, *51*(9), 1209–1223, doi:10.1007/s11430-008-0097-1.
Zhao, Y., Z. Yu, and W. Zhao (2011), Holocene vegetation and climate histories in the eastern Tibetan Plateau: Controls by insolation-driven temperature or monsoon-derived precipitation changes?, *Quat. Sci. Rev.*, *30*(9–10), 1173–1184, doi:10.1016/j.quascirev.2011.02.006.
Zheng, Y., W. Zhou, P. A. Meyers, and S. Xie (2007), Lipid biomarkers in the Zoigê-Hongyuan peat deposit: Indicators of Holocene climate changes in West China, *Org. Geochem.*, *38*(11), 1927–1940, doi:10.1016/j.orggeochem.2007.06.012.
Zhou, W., X. Lu, Z. Wu, L. Deng, A. J. T. Jull, D. Donahue, and W. Beck (2002), Peat record reflecting Holocene climatic change in the Zoige Plateau and AMS radiocarbon dating, *Chin. Sci. Bull.*, *47*(1), 66–70.
Zielke, O., J. R. Arrowsmith, L. Grant Ludwig, and S. O. Akçiz (2010), Slip in the 1857 and earlier large earthquakes along the Carrizo Plain, San Andreas Fault, *Science*, *327*(5969), 1119–1122, doi:10.1126/science.1182781.
Zielke, O., Y. Klinger, and J. R. Arrowsmith (2015), Tectonophysics Fault slip and earthquake recurrence along strike-slip faults—Contributions of high-resolution geomorphic data, *Tectonophysics*, *638*, 43–62, doi:10.1016/j.tecto.2014.11.004.